Optimal Design of Nonlinear Periodic Electrical Networks for Soliton Pulse Generation

by

Andrew Gusty

A Senior Thesis submitted to the
University of Colorado Boulder
in partial fulfillment of the requirements for the degree of
Bachelor of Science

Department of Applied Mathematics and Computer Science

Advising Committee:
Dr. Elizabeth Bradley
Dr. Fruzsina Agocs
Dr. Emily Jensen
Dr. Cody Scarborough

April 7, 2026

Abstract

Nonlinear transmission lines (NLTLs) provide a practical platform for generating high-power, ultrashort electrical pulses, but their design remains largely heuristic and relies on continuum approximations for small-amplitude pulses. This work develops a computational framework for designing NLTLs that support localized, large-amplitude solitons directly at the level of the discrete lattice dynamics. Starting from an LC-ladder model, with voltage-dependent capacitors, we formulate the problem of selecting NLTL parameters as an optimization over traveling-wave solutions of the infinite lattice dynamics. Motivated by high-power ultrawideband applications, an objective, based on the spread of the pulse's energy, is introduced to quantify pulse localization. Feasible solutions are found numerically to lie on a one-dimensional curve in the parameter space, with larger solitons observed to be more localized. Time-domain simulations of the found solutions propagating through the lattice show that these appear dynamically stable. In addition, we show through numerical experiments that a trapezoidal pulse on the NLTL evolves into a train of localized pulses with amplitude-dependent speeds. These findings provide evidence that large-amplitude solitary waves exist in discrete NLTLs and are asymptotically stable.

Acknowledgments

I would like to thank Professor Emily Jensen and Professor Cody Scarborough for their guidance throughout this project. Much of what I understand about nonlinear systems as an undergraduate comes from working with them, and their mentorship has shaped how I approach both modeling and analysis. They helped develop the thesis topic and have guided my research over the past two years.

I am also very grateful to Professor Elizabeth Bradley and Professor Fruzsina Agocs for serving on my committee and for their support and feedback during our meetings, which helped improve the clarity and presentation of the thesis.

I would also like to thank some of the students who made research especially enjoyable. Addie McCurdy, Isabel Collins, and Sam Smith have spent many hours helping me work through problems, and Cody Oberbeck's advice was very helpful in designing the experiments presented in this thesis.

Finally, I would like to acknowledge the support of the University of Colorado Boulder College of Engineering and Applied Science, which provided the resources necessary to carry out this work.

Contents

List of Tables

List of Figures

1. Introduction

The generation of ultrashort microwave pulses is required by many ultrafast and ultrabroadband technologies [1, 2]. At high peak power levels, pulsed UWB signals have many advantages for use in radar systems [3, 4] and medical imaging [5]. At low powers, UWB has been of recent interest for communications and sensor-networks [6]. In these pulsed UWB systems, it is highly desirable to generate short, localized pulses with shorter rise times [1].

For this purpose, nonlinear transmission lines (NLTL) have emerged as promising platforms for synthesizing broadband, high-frequency pulses from low-frequency input waveforms [7, 8, 9]. Compared to established vacuum and e-beam devices, NLTLs offer lower costs, accessible manufacturing, and can theoretically provide both high-power and high-frequency wideband operation [7, 10, 11]. Using an NLTL-based solid-state modulator has several advantages over standalone e-beam devices [7, 12, 8]. Because NLTLs have no moving parts, they enjoy greater reliability and lower maintenance requirements than more complex devices. In addition, transmission line components have a high degree of manufacturing maturity and wide availability of components, while also allowing for more compact and modular designs.

NLTLs traditionally were used to modulate pulses mainly by decreasing the rise-time of an input pulse [13, 14]. This modulation is made possible by the phase velocity, or speed of individual Fourier components propagating along a line, being directly related to their amplitude. On an NLTL with voltage-dependent capacitors or inductors, large-amplitude components move faster than small-amplitude components, which can be exploited to sharpen an input pulse [15].

More recently, there has been great interest in the use of NLTLs for synthesizing high-power RF signals, following two experimental studies. In the first, an NLTL with voltage-dependent ceramic capacitors was used to produce 60 MW peak RF power at 100-200 MHz [9]. The second study used nonlinear inductors and linear capacitors in an NLTL-based modulator to produce 20 MW peak power at 1.0 GHz [8]. This device was the precursor to the current NLTL-based solid-state modulator sold by BAE systems, which produces over 25 MW peak power at 200 MHz - 2.0 GHz [12].

RF-pulse generation using NLTLs is accomplished by inputting a low-frequency, low-power waveform into an NLTL, and extracting the modulated signal after it has propagated through the system. As the pulse moves along the line, it evolves into a train or burst of sharp, stable pulses [7, 11, 16, 8], called *solitons* - special waveforms that propagate along an NLTL without distortion. The output burst has a significantly broader and higher spectrum than the input pulse, making it suitable for UWB contexts [7]. The effects of changing dispersion, line length, and type of nonlinearity have been experimentally investigated in [10, 11]. Some basic analytical expressions for the RF amplitude, the maximum voltage, and the central frequency of the generated pulses at each node of an NLTL have also been formulated using curve-fitting from experimental data in [16].

However, a major barrier to deploying NLTLs in other high-power systems is the absence of a systematic framework for tuning an NLTL's parameters to synthesize solitons with desired power, spectral content, and pulse width. A general method for designing NLTLs would give insight into the limits of pulse modulation using solid-state devices, and would enable the expansion of NLTLs to new UWB applications.

Optimizing the parameters of an NLTL is difficult because the equations governing the voltage dynamics of NLTL pulse propagation in discrete space are described by large systems of coupled nonlinear ODEs. In the case of an electrically long and weakly dispersive transmission line, the dynamics can be closely approximated by high-order nonlinear and dispersive wave equations on an infinite domain. For a long transmission line loaded by voltage-dependent capacitors, the dynamics of a small-amplitude pulse can be further reduced to the Korteweg-de Vries (KdV) equation [15, 7], which admits a family of stable, closed-form *solitary wave* solutions that give precise relations between the parameters of the NLTL and the soliton waveform it supports. In addition, the family of solitary wave solutions is asymptotically stable [17] with respect to a properly-weighted norm. One of the implications of this stability is that a sufficiently smooth initial pulse will converge to one or more soliton solutions in a traveling reference frame for the KdV equation [15, 18, 19, 17].

However, continuum approximations are limited to long-wavelength, small-amplitude pulses, and therefore do not capture the short, high-power pulses required in practical pulsed UWB systems. As a result, their direct applicability to ultrafast and high-power NLTL pulse synthesis is limited. Nevertheless, experiments at practical operating powers and frequencies show promising stability results: an input pulse evolves into a train of stable soliton pulses [7, 8, 9]. This suggests that the mechanisms that lead to soliton formation in small-amplitude theory may persist in large-amplitude regimes where no analytical description is currently available.

The goal of this work is to develop a systematic framework for designing NLTLs that support short, high-power soliton pulses beyond the small-amplitude regime. Rather than relying on asymptotic approximations, we study the discrete lattice dynamics directly and formulate the pulse synthesis problem in terms of the solitary-wave solutions supported by the network.

Specifically, we formulate the pulse synthesis problem for NLTLs as an optimization problem over solitary-wave solutions, using a physically motivated objective that measures the concentration of energy in the traveling frame. The goal of this optimization problem is to determine NLTL parameter values that support short, high-power soliton pulses with minimal energy spread. We solve this optimization problem numerically and show that, in the large-amplitude regime, soliton solutions persist and can be systematically selected through parameter tuning. In particular, we observe numerically that optimizing over the system parameters is equivalent to selecting the amplitude of a desired soliton pulse, which is inversely related to pulse width. This provides a direct connection between circuit design and waveform properties.

To assess the relevance of these solutions for pulse synthesis, we then investigate their stability and dynamical behavior in the full discrete system. Using time-domain simulations based on a symplectic integration scheme, as well as circuit-level validation in a commercial solver, we demonstrate that the optimized soliton profiles propagate stably and retain their structure over long distances. In addition, we present numerical experiments showing that broad input waveforms evolve into trains of short, localized soliton pulses, consistent with the behavior observed in high-power NLTL experiments. These results provide evidence that the optimized solitary-wave solutions can be realized dynamically and used for high-power pulse generation.

The remainder of this thesis is organized as follows. In Section 2, we introduce the nonlinear transmission line model and derive the governing equations for the LC-ladder network. Section 3 reviews the small-amplitude approximation and the KdV equation as a conceptual model for soliton formation, and highlights its limitations for short, high-power pulses. In Section 4, we formulate the optimization problem and develop the numerical approach used to identify parameter regimes that support localized, large-amplitude soliton pulses. Section 5 presents numerical experiments demonstrating the stability and dynamical realization of these pulses in both the discrete lattice and circuit-level simulations. We conclude in Section 6 with a discussion of the results and directions for future work.

2. Nonlinear Transmission Line Model

Nonlinear transmission lines (NLTLs) are most commonly modeled as LC-ladder networks, where inductors connect neighboring nodes and nonlinear capacitors are connected to ground [7, 10, 11, 14, 15, 16, 1]. These models are used because they are made of widely available standard circuit elements and have simple physics which admits analytical results.

More generally, NLTLs can be viewed as periodic electrical networks composed of repeated unit cells that include both linear and nonlinear elements. For example, distributed transmission lines and coplanar waveguides loaded with nonlinear capacitors have also been shown to support soliton-like waveforms [20]. In addition, practical designs may use non-uniform unit cells with slowly varying parameters to achieve specific waveform shaping objectives, such as reducing the rise time of an input pulse [13]. Finally, designs that use linear capacitors and nonlinear inductors [8, 12], have also been shown to be useful in pulse generation for UWB applications.

In this work, we restrict attention to uniform LC-ladder networks with nonlinear capacitors and linear inductors. This choice is motivated by the fact that LC-ladder models admit a well-developed analytical description in the small-amplitude regime, where the dynamics reduce to the KdV equation, as will be discussed in Section 3. In this setting, the mechanisms underlying pulse propagation, including the formation of solitary waves and their amplitude-dependent speeds, are understood rigorously. The goal of this work is to take the first step in investigating whether these same mechanisms persist outside the small-amplitude regime, where the analytical approximation is no longer valid. By working within the LC-ladder framework, we retain a direct connection to the existing theory while extending the analysis to a regime where little is known. This provides a controlled setting in which the numerical methods developed here can be validated before considering more general NLTL designs.

The key physical mechanisms governing NLTL behavior are dispersion and nonlinearity strength. Dispersion arises from the discrete structure of the network: because signals propagate through a sequence of unit cells, different frequency components travel at different speeds. As a result, waves tend to spread out over time as they propagate through a discrete, linear network. Nonlinearity, introduced through voltage-dependent circuit elements, causes the propagation speed to depend on the amplitude of the signal. In many NLTL designs, larger-amplitude portions of a waveform travel faster than smaller-amplitude portions, leading to waveform steepening.

Individually, both dispersion and nonlinearity tend to distort signals as they propagate. However, under certain conditions, these effects can “balance”. When nonlinear steepening is offset by dispersive spreading, stable, localized traveling pulses can propagate without distortion. In Section

3, we show that for small-amplitude waves, dispersive and nonlinear effects must both be weak. We refer the reader to Ch. 2-3 in [15] for a more detailed discussion of these effects.

2.1 LC-Ladder Network

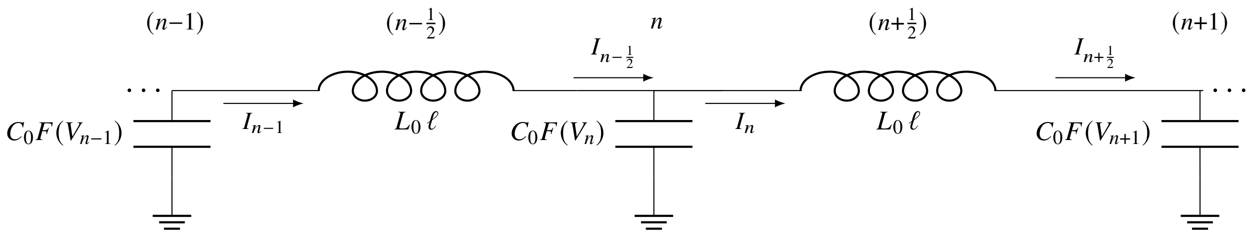

Figure 1: Circuit diagram of an LC-ladder network with linear inductors and voltage-dependent capacitors.

A standard and physically realizable NLTL model is the LC-ladder network, shown in Fig. 1, in which each unit cell consists of a series inductor and a shunt voltage-dependent capacitor [10, 14, 15]. In this setting, the discrete spatial structure of the line produces dispersion, while the nonlinear capacitor introduces amplitude dependence into the wave speed. Later sections show how these two effects can balance to support solitary traveling pulses.

We consider an infinite, spatially uniform ladder indexed by $n \in \mathbb{Z}$, with unit-cell length $\ell > 0$. The series inductance in each cell is ℓL_0, where L_0 has units of inductance per unit length, and the charge and capacitance at node n are modeled as

$$Q_n = C_0 \int_0^{V_n} F(s)\, ds, \qquad C(V_n) = \frac{dQ_n}{dV_n} = C_0 F(V_n) \tag{1}$$

where C_0 is the reference capacitance per unit cell and F is a dimensionless nonlinear function. The model parameters used throughout this section are summarized in Table 1. We define the antiderivative

$$G(V) = \int_0^{V} F(s)\, ds = \frac{\gamma}{1-m}\left(\left(1 + \frac{V}{\gamma}\right)^{1-m} - 1\right), \tag{2}$$

so that the charge and capacitance are given by

$$Q_n = C_0 G(V_n), \qquad C(V_n) = \frac{dQ_n}{dV_n} = C_0 F(V_n). \tag{3}$$

Parameter	Description	Units
L_0	Inductance per unit length	H/m
C_0	Reference capacitance per unit cell	F
ℓ	Unit-cell length	m
$Z_0 = \sqrt{\ell L_0 / C_0}$	Reference characteristic impedance	Ω
$C(V)$	Voltage-dependent capacitance of one shunt element	F
Q_n	Charge stored in the n^{th} capacitor	C
Φ_n	Magnetic flux through the n^{th} inductor	$\mathrm{V \cdot s}$

Table 1: Parameter definitions for the LC-ladder network with voltage-dependent capacitors.

Let $t \in [0, T] \subset \mathbb{R}$ denote time. The real voltage at node n is denoted by

$$V_n : [0, T] \to \mathbb{R}, \tag{4}$$

and the real current through the series inductor between nodes n and $n + 1$ is denoted by

$$I_n : [0, T] \to \mathbb{R}, \tag{5}$$

with the positive direction taken from node n to node $n + 1$.

To derive the governing equations, we introduce the magnetic flux $\Phi_n(t)$ through the inductor between nodes n and $n+1$, and the charge $Q_n(t)$ stored in the capacitor at node n. These are defined by

$$\Phi_n(t) = \ell L_0 I_n(t), \tag{6}$$

$$Q_n(t) = C_0 \int_0^{V_n(t)} F(s)\, ds = C_0 G\big(V_n(t)\big) \tag{7}$$

The first identity is the usual inductor constitutive relation written in flux form. The second reflects the charge-voltage law of the nonlinear capacitor under the choice $C(V) = C_0 F(V)$.

Applying Kirchhoff's voltage law across the inductor between nodes n and $n + 1$ gives

$$V_n(t) - V_{n+1}(t) = \frac{d}{dt}\Phi_n(t). \tag{8}$$

Using $\Phi_n = \ell L_0 I_n$, this becomes

$$V_n - V_{n+1} = \ell L_0 \frac{dI_n}{dt}. \tag{9}$$

Writing (9) for the inductors indexed by $n - 1$ and n and subtracting yields

$$V_{n-1} - 2V_n + V_{n+1} = \ell L_0 \frac{d}{dt}\left(I_{n-1} - I_n\right). \tag{10}$$

Next, Kirchhoff's current law at node n gives

$$I_{n-1}(t) - I_n(t) = \frac{dQ_n}{dt}. \tag{11}$$

Substituting (11) into (10) and using (7) yields the discrete evolution equation

$$V_{n-1} - 2V_n + V_{n+1} = \ell L_0 C_0 \frac{d^2}{dt^2}\big[G(V_n)\big] \tag{12}$$

Equation (12) is the governing lattice equation for the nodal voltages of the infinite LC-ladder network.

The nonlinear capacitance arises from voltage-dependent charge storage mechanisms in devices such as varactor diodes. The function $F(V)$ captures the nonlinear voltage dependence. In this work, we take

$$F(V) = \frac{1}{\left(1 + \frac{V}{\gamma}\right)^m}, \qquad \gamma > 0, \quad 0 < m < 1. \tag{13}$$

This functional form is commonly used to model voltage-dependent capacitors [1, 21]. It is motivated by the voltage-dependent junction capacitance of a reverse-biased p–n junction [22], for which the capacitance decreases as the reverse bias increases. In this model, γ is a characteristic voltage scale associated with the junction potential, while the exponent m is the grading coefficient determined by the junction profile. For example, abrupt junctions typically correspond to $m \approx 1/2$.

This class of models is useful in NLTL analysis because it gives a simple closed-form approximation of measured capacitance-voltage curves while retaining the nonlinear effect responsible for pulse sharpening, pulse compression, and solitary-wave formation.

2.2 LC-Ladder Pulse Synthesizer Model

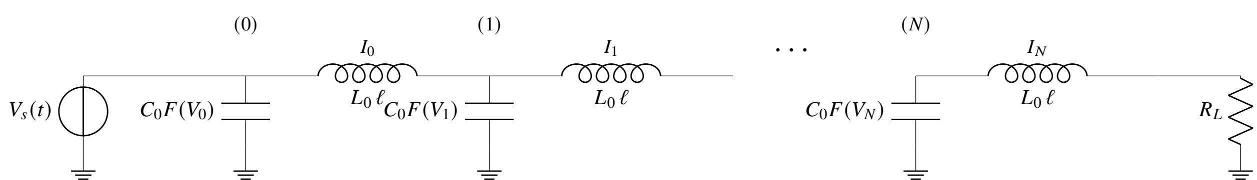

Figure 2: Pulse synthesizer based on a finite nonlinear LC-ladder driven by an ideal voltage source and terminated by a resistive load R_L.

The pulse synthesis process is carried out on a finite ladder network, in which an input waveform is applied at one boundary, propagated through a finite number of unit cells, and extracted at a terminating load. The resulting system, shown in Fig. 2, consists of $N + 1$ nodes indexed by $n = 0, 1, \ldots, N$, with currents $I_n(t)$ flowing between nodes n and $n + 1$ for $n = 0, \ldots, N$.

The interior dynamics are governed by the same discrete evolution equation derived for the infinite lattice. In particular, for $n = 1, \ldots, N$,

$$V_{n-1} - 2V_n + V_{n+1} = \ell L_0 C_0 \frac{d^2}{dt^2}\big[G(V_n)\big], \tag{14}$$

where each term in the above equation is defined in Section 2.1. Thus, away from the boundaries, the finite system evolves according to the same local interaction laws as the infinite network.

The system is closed by boundary conditions at the input and output nodes. At the left boundary, the applied voltage source prescribes the nodal voltage,

$$V_0(t) = V_s(t), \tag{15}$$

which serves as a time-dependent boundary input.

At the right boundary, the load resistor relates the terminal voltage and current through

$$V_{N+1}(t) = R_L I_N(t). \tag{16}$$

Using the inductor relation (9) to eliminate I_N yields

$$\frac{dV_{N+1}}{dt} = \frac{R_L}{\ell L_0}\big(V_N - V_{N+1}\big), \tag{17}$$

which provides a dynamical boundary condition at the output.

Equations (14)–(17) define a finite-dimensional nonlinear dynamical system driven by the input waveform $V_s(t)$. Since the system is second order in time, it is supplemented with initial data for the interior nodes,

$$V_n(0), \qquad \frac{dV_n}{dt}(0), \qquad n = 1, \ldots, N. \tag{18}$$

For sufficiently long ladders, the interior dynamics are well approximated by those of the infinite lattice over time periods prior to the pulse interacting with the right termination boundary. In this regime, we aim to study localized, traveling soliton pulses. This motivates the use of traveling-wave solutions of the infinite lattice as a reduced description of pulse propagation in the finite system.

Remark. In the linear setting, a non-reflecting boundary is obtained by impedance matching. The load is chosen so that the voltage and current at the boundary satisfy a fixed proportionality determined by the characteristic impedance. This condition eliminates reflections of traveling waves. In the nonlinear lattice, the relationship between voltage and current for a propagating wave depends on the amplitude and structure of the waveform, and cannot be represented by a fixed proportionality. A constant resistive load therefore cannot enforce the correct boundary relation for a nonlinear traveling wave and does not eliminate reflections. A perfectly non-reflecting boundary corresponds to a transparent boundary condition that enforces purely outgoing waves. For discrete nonlinear systems, such conditions are nonlocal in time and depend on the past history of the waveform [23]. These types of operators are nontrivial to implement using standard circuit elements. For these reasons, practical NLTL implementations use constant resistive terminations [24, 7, 1], which provide only approximate matching and generally lead to reflections at the boundary.

To isolate the conservative dynamics of the ideal lossless LC-ladder from the losses and reflections incurred by the mismatched boundary, the analysis in this work focuses on the evolution of pulses prior to their interaction with the boundary. This way, the dynamics of the measured signals are governed predominantly by the intrinsic properties of the lattice rather than boundary effects.

2.3 Nondimensionalization

To reduce the number of parameters in the dynamics and identify the governing relationships between parameters to simplify the analysis, we nondimensionalize the dynamics. Let

$$\tau = \frac{t}{\sqrt{\ell L_0 C_0}}, \qquad \chi = \frac{x}{\ell} = n, \qquad \phi = \frac{V}{V_c}, \tag{19}$$

where V_c is a characteristic voltage scale.

The time scaling $\sqrt{\ell L_0 C_0}$ represents the natural timescale of the circuit linearized about $V = 0$, while ℓ is the spatial scale of each unit cell. This corresponds to a characteristic linear wavespeed

$$c_{\text{lin}} = \sqrt{\frac{\ell}{L_0 C_0}}, \tag{20}$$

Since stable solitons have stationary profile in a moving frame, we further introduce a nondimensional traveling coordinate

$$\xi = \frac{1}{\ell}(n\ell - ct) = \chi - \bar{c}\,\tau, \tag{21}$$

where the (assumed constant) nondimensional wave speed is

$$\bar{c} = c\sqrt{\frac{L_0 C_0}{\ell}} = \frac{c}{c_{\text{lin}}}. \tag{22}$$

The traveling coordinate can be physically interpreted as fixing a spatial index n on the infinite LC-ladder and viewing the waveform measured at that index as a function of time (extending to $\xi \to \pm\infty$), with the pulse centered at $\xi = 0$. We note that in the above nondimensionalization, V_c is a free variable in the dynamics. Since we study soliton pulses, set $V_c = \|V_n(t)\|_{L_\infty}$ as the pulse amplitude so that the nondimensional pulse has amplitude $\phi(0) = 1$ (for a pulse centered in the moving frame). Under these scalings, searching for a traveling wave solution with constant profile $\phi(\xi)$ reduces the governing equation to

$$\phi(\xi - 1) - 2\phi(\xi) + \phi(\xi + 1) = \bar{c}^2 \frac{d^2}{d\xi^2}\big[G(\phi(\xi))\big], \tag{23}$$

where $G(V)$ is the anti-derivative with respect to ϕ of the capacitance model,

$$F(\phi) = \frac{1}{\left(1 + \frac{\phi}{b}\right)^m}, \qquad b = \frac{\gamma}{V_c}, \tag{24}$$

we see that the system is governed by three key nondimensional parameters:

$$\bar{c}\ \ \text{(wave speed)}, \qquad b\ \ \text{(nonlinearity scale)}, \qquad m\ \ \text{(grading coefficient)} \tag{25}$$

These parameters determine the shape and propagation properties of traveling pulses in the nonlinear transmission line. In practice, m is a property of the capacitors used, and is fixed after manufacturing. On the other hand, $\bar{c}$ and b can be tuned after manufacturing by changing the length of unit cells (ℓ) or the (dimensional) amplitude of the pulse (V_c), and before manufacturing by changing other circuit parameters. Because $\bar{c}$ and b can be tuned after manufacturing, we focus on optimizing these two parameters.

3. The Small-Amplitude Approximation

For a very long network in which each linear component is electrically small relative to the wavelength of the propagating pulse, the discrete lattice behaves approximately as a continuum [15]. Using the perturbation analysis in Appendix A, the voltage dynamics reduce, at leading order in the weakly nonlinear, long-wavelength regime, to the Korteweg–de Vries (KdV) equation

$$U_T + \frac{\alpha}{2} U U_X + \frac{1}{24} U_{XXX} = 0. \tag{26}$$

where U is the voltage to leading order,

$$V(x,t) = \epsilon U(X,T) + O(\epsilon^2),$$

and the slow variables X and T are defined in Appendix A. The KdV equation admits a closed-form solitary-wave solution; for completeness, this solution is derived in Appendix B.

The derivation of (26) requires two independent assumptions:

1. **Long wavelength:** the pulse width is much larger than the cell length ℓ, so that the Taylor expansion of the discrete Laplacian is accurate.
2. **Small amplitude:** the voltage remains sufficiently small that the quadratic truncation

   $$F(V) = 1 - \alpha V + O(V^2/\gamma^2)$$

   is valid. In terms of the nondimensional parameters in Section 2.3, this requires

   $$\frac{|V_c|}{\gamma} = \frac{1}{b} \ll 1.$$

The long wavelength of the pulse allows the continuum approximation to hold, and corresponds with weak dispersion. The small-amplitude approximation corresponds with weak nonlinearity. This matches the intuition that the dispersion and nonlinearity must "balance" to support a soliton. Accordingly, the KdV equation (26) is not an exact model for the lattice, nor does it describe large-amplitude solitary waves in the discrete system. Rather, it is the leading-order asymptotic model of weakly nonlinear, weakly dispersive lattice dynamics.

Despite this restrictive regime, the KdV equation provides a remarkably complete description of the qualitative mechanisms that motivate the experiments in Section 5. Early work by Ablowitz and Segur [18] established the long-time behavior of solutions arising from localized initial data. They showed that, in the absence of solitons, the solution does not remain localized, but instead evolves into a purely dispersive structure with several asymptotic regions, including oscillatory decay and a collisionless-shock layer. This result highlights a fundamental feature of dispersive systems: not all initial energy organizes into coherent structures, and a portion of the solution spreads out over time.

Building on this, Schuur [19] gave one of the first rigorous descriptions of how solitons emerge from general rapidly decaying initial data. He showed that when solitons are present, the long-time solution separates into a finite train of solitary waves together with a dispersive remainder. The solitons are ordered by speed, with larger-amplitude pulses traveling faster and moving ahead of smaller ones. For the present work, this provides a model example of the phenomenon sought later in the discrete NLTL: a broad input waveform evolving into a sequence of localized output pulses.

A natural question is whether these solitary waves persist or whether they are only transient features. For the KdV equation, Pego and Weinstein proved that the one-soliton family is asymptotically stable [17]. Specifically, if a solution starts sufficiently close to a solitary wave, then it converges, in a frame moving with the pulse, to a nearby solitary wave with slightly adjusted parameters, while the remaining perturbation disperses. Importantly, this convergence holds in a weighted sense: the dispersive component does not vanish, but instead spreads out and becomes negligible near the core of the pulse. This result is consistent with the earlier works of Ablowitz–Segur and Schuur, which show that dispersive radiation persists but separates spatially from the coherent soliton structures.

Taken together, these results show that localized input pulses may decompose into solitons plus dispersive radiation, that larger solitons travel faster, and that individual solitons are asymptotically stable in the sense that perturbations disperse away from the pulse. These are precisely the qualitative features tested later in the numerical experiments.

At the same time, the assumptions required to reach the KdV regime make it poorly suited for pulse synthesis in certain applications. In particular, UWB pulsed-radar systems require ultrashort pulses with high frequency and power content [1, 3]. In contrast, the small-amplitude condition $1/b \ll 1$ implies that the voltage scale is small relative to the nonlinearity scale γ, so the pulse carries relatively little power. The long-wavelength assumption implies that the pulse width is large relative to the unit-cell length, so the resulting waves are broad rather than sharply localized. In other words, the small-amplitude approximation describes low-power, wide pulses, whereas the applications motivating this thesis require short, high-peak-power pulses with strong temporal localization. This motivates our investigation beyond the small-amplitude regime to study large-amplitude solitary waves directly for the discrete lattice dynamics.

4. Optimization Problem

4.1 Energy and Power Metrics

Motivated by UWB applications, our goal is to examine solitons beyond the small-amplitude regime. Since the small-amplitude regime corresponds to a low-power, wide signal, we focus on UWB radar applications, where short pulses with high peak power for a finite amount of energy are desired [3, 1]. To support a high pulse repetition rate, it is also important that pulses are localized with minimal ringing [1], meaning that they decay quickly and smoothly away from their peak.

With these considerations in mind, we seek a principled way to compare profiles that solve the nonlinear lattice dynamics in (23). Under the principle that dispersive effects must balance with nonlinear ones to support a soliton, we anticipate that large-amplitude solitons (if they exist) will have short pulse widths and steep rise-times. This motivates posing an optimization problem to identify pulses with energy concentrated near their peak.

To study the intrinsic properties of the solitary waves supported by the lattice, we formulate the optimization problem for the pulses supported by the infinite LC-ladder (Fig. 1) rather than the finite-length pulse synthesizer (Fig. 2). This is because the waveform extracted from the finite-length pulse synthesizer depends on the choice of termination.

Ideally, the pulse-synthesizer's termination acts as a transparent boundary condition and perfectly extracts the soliton. However, due to the nonlinear effects, a transparent boundary condition requires a termination with voltage-dependent impedance (as opposed to a constant impedance), which is nontrivial to implement with basic circuit components. As a result, the impedance is often approximated using a constant resistor at the boundary [24, 7]. Since our objective is to characterize the solitary-wave profiles themselves, independent of these boundary effects, we assume that some suitable termination strategy can be employed and work with the incident pulse on a nonreflecting infinite line.

Under this assumption, we optimize using the incident energy carried by the pulse before it reaches the boundary. For a lossless lattice with uniform unit cells, the incident energy and corresponding instantaneous power are,

$$E_{\text{inc}} = \int_{-\infty}^{\infty} V_n(t)\, I_n(t)\, dt, \qquad P(t) = V_n(t) I_n(t). \tag{27}$$

For a soliton on a lossless NLTL, the incident energy is independent of the lattice index n [24]. Substituting the expression in (9) for I_n in terms of V_n, passing to the traveling-wave coordinate, and rewriting in terms of the nondimensional voltage profile ϕ, this becomes

$$E_{\text{inc}} = \frac{V_c^2 C_0}{\bar{c}^2} \int_{-\infty}^{\infty} \phi(\xi) \int_{-\infty}^{\xi} \big[\phi(s) - \phi(s+1)\big]\, ds\, d\xi. \tag{28}$$

We define the corresponding power in the traveling coordinate as

$$P(\xi) = V_c^2 \frac{\sqrt{C_0}}{\bar{c}\sqrt{\ell L_0}}\, \phi(\xi) \int_{-\infty}^{\xi} \big[\phi(s) - \phi(s+1)\big]\, ds, \tag{29}$$

and normalize it by the incident energy using

$$p(\xi) = \frac{\phi(\xi) \int_{-\infty}^{\xi} \big[\phi(s) - \phi(s+1)\big]\, ds}{\int_{-\infty}^{\infty} \phi(\xi) \int_{-\infty}^{\xi} \big[\phi(s) - \phi(s+1)\big]\, ds\, d\xi} \tag{30}$$

Note that by construction,

$$\int_{-\infty}^{\infty} \frac{P(t)}{E_{\text{inc}}} dt = \int_{-\infty}^{\infty} \frac{P(\xi)}{E_{\text{inc}}} \Big(\frac{\sqrt{\ell L_0 C_0}}{\bar{c}}\, d\xi \Big) = \int_{-\infty}^{\infty} p(\xi) d\xi = 1. \tag{31}$$

so $p(\xi)$ may be interpreted as a distribution of energy density in the traveling coordinate. Thinking of $p(\xi)$ informally as a probability distribution, we define the mean location of the pulse as the first moment of $p(\xi)$:

$$\bar{\xi}[\phi(\xi)] = \int_{-\infty}^{\infty} \xi\, p\big(\phi(\xi), \xi\big)\, d\xi, \quad \bar{\xi} : \tag{32}$$

and the variance as

$$\sigma^2[\phi(\xi)] = \int_{-\infty}^{\infty} (\xi - \bar{\xi})^2 p\big(\phi(\xi), \xi\big)\, d\xi. \tag{33}$$

We use the bracket notation $\sigma^2[\cdot]$, $\bar{\xi}[\cdot]$ to denote that σ^2 and $\bar{\xi}$ are functionals which map a function to a real number that measures how concentrated the energy of the pulse is around its peak. We adopt the variance as a heuristic objective because, for fixed incident energy, smaller variance corresponds to a more localized energy distribution. This favors pulses with shorter effective duration, penalizes energy away from the peak (i.e., ringing), and consequently yields pulses with higher peak power.

Remark: We note that the definitions of energy and power in (27) are dimensional and originate from the physical time-domain quantities $V_n(t)$ and $I_n(t)$. In contrast, the mean and variance $\bar{\xi}$ and σ^2 are nondimensional and are defined in the nondimensional coordinate ξ, rather than in time t. This choice is deliberate. Since the reduced traveling-wave problem is posed in the coordinate ξ, the quantity σ^2 measures the concentration of the solitary-wave profile itself. If variance were defined directly in physical time, it would depend not only on the shape of the traveling-wave profile, but also on the rate at which that profile moves past a fixed observation point. In other words, the same profile would appear more temporally concentrated simply because it propagates faster. By defining the objective in ξ, we instead measure the intrinsic concentration of the waveform profile itself, without introducing this additional dependence on propagation speed.

4.2 Pulse Synthesizer Optimization Problem

Before introducing the reduced optimization problem for solitary waves on an infinite lattice, we first formulate the physically relevant design problem for the finite-length pulse synthesizer described in Fig 2. Recall that the finite LC-ladder consists of nodes indexed by $n = 0, 1, \ldots, N$, (where $N \gg 1$ for a long NLTL) whose interior dynamics are governed by (14), with boundary conditions given by the input voltage

$$V_0(t) = V_s(t),$$

and the resistive termination at the right boundary,

$$V_{N+1}(t) = R_L I_N(t),$$

or equivalently (17) after eliminating the current. This defines a finite-dimensional nonlinear dynamical system that maps an input waveform $V_s(t)$, physical parameters (which we denote with the vector $\boldsymbol{p}$), and output termination R_L, to an output waveform $V_{N+1}(t)$ at the terminal node.

At this level, the design objective is to produce an output pulse with desirable characteristics, such as short temporal support, high peak power, and minimal ringing. To formalize this using the same variance idea from the previous section, let

$$V_{N+1}(t; V_s, \boldsymbol{p}, R_L)$$

denote the terminal voltage generated by the finite ladder, where

$$\boldsymbol{p} = (L_0, C_0, \ell, \gamma, \ldots)$$

collects the physical parameters of the transmission line, and $R_L > 0$ is the load resistance. A general formulation of the pulse synthesis problem is then given by

$$\min_{V_s(\cdot),\, \boldsymbol{p},\, R_L} \ \sigma^2_{\text{fin}}[V_{N+1}(\cdot; V_s, \boldsymbol{p}, R_L)] \quad \text{subject to} \quad (14)\text{–}(17), \tag{34}$$

where σ^2_{fin} is a functional defined on time-domain signals that quantifies the quality of the extracted pulse.

This formulation highlights that pulse synthesis involves three coupled design components: (i) selection of the lattice parameters $\boldsymbol{p}$, which determine the nonlinear dispersive dynamics of the line, (ii) design of the injected waveform $V_s(t)$, which excites those dynamics, and (iii) choice of the termination R_L, which governs how the pulse is extracted at the boundary. These components are strongly coupled through the nonlinear finite-domain dynamics. The coupling of the design variables means that the optimization requires simultaneously selecting a boundary input, system parameters, and termination through a nonlinear dynamical map.

Even for fixed parameters $(\boldsymbol{p}, R_L)$, determining an input waveform $V_s(t)$ that produces a desired output waveform $V_{N+1}(t)$ constitutes a nonlinear inverse problem. The map $V_s \mapsto V_{N+1}$ is defined implicitly through the finite-dimensional nonlinear dynamics (14)–(17), and in general cannot be expressed in closed form.

For these reasons, rather than attempting to solve (34) directly, we instead seek a reduced formulation that isolates the intrinsic waveform properties supported by the transmission line, independent of the particular choice of input waveform and boundary termination.

To obtain a tractable formulation, we approximate the finite lattice over time periods prior to interaction with the right boundary by the corresponding infinite system. For sufficiently large N, and for times during which the injected waveform has not yet reached the termination, the dynamics of the finite system are well approximated by those of the infinite lattice. This allows us to study the intrinsic waveform dynamics supported by the transmission line independently of boundary effects.

We now state the assumptions that justify reducing the pulse synthesis problem to an optimization over solitary-wave solutions of the infinite lattice. These assumptions are motivated by the asymptotic stability results of the small-amplitude approximation discussed in Section 3 and are supported by numerical observations in Section 5.

Hypothesis 1 (Existence of localized traveling waves). For the traveling-wave equation (23) posed on the infinite lattice with decay conditions $\lim_{\xi\to\pm\infty} \phi(\xi) = 0$, and nonlinearity $F(\phi)$ specified in (24), for fixed parameters $0.5 \le m < 1$ and $b > 0$, there exists a wavespeed $\bar{c} > 1$ such that a nontrivial localized traveling-wave solution $\phi(\xi)$ exists.

Hypothesis 2 (Asymptotic decomposition into solitary waves). For a class of sufficiently smooth, localized input waveforms $V_s(t)$, the solution of the infinite lattice evolves, for large times, into a superposition of finitely many spatially separated solitary traveling waves together with a dispersive remainder. Each solitary wave propagates with constant profile and speed determined by its amplitude, and is stable under perturbations in an appropriate moving frame.

Hypothesis 3 (Amplitude selection by input waveform). The amplitudes of the solitary waves arising in the asymptotic decomposition depend continuously on the injected waveform $V_s(t)$. In particular, varying the amplitude and shape of $V_s(t)$ allows one to select the amplitude of the largest solitary wave generated by the system.

These hypotheses are not established rigorously for the present system and are therefore treated as modeling assumptions. However, they are consistent with the asymptotic stability results of the KdV equation, and are supported by the numerical experiments presented in Section 5.

Under these assumptions, the dynamics of the system prior to interaction with the boundary are governed by the family of solitary traveling waves supported by the infinite lattice. In turn, the family of solitary waves is parameterized by the dimensional amplitude V_c. In contrast, the injected waveform $V_s(t)$ and termination R_L determine which of these solitary waves is generated by the pulse synthesizer.

This observation suggests that the pulse synthesis problem may be decomposed conceptually into two components: (i) selecting the parameter values that yield desirable solitary-wave profiles, and (ii) determining the input and termination conditions that generate a solitary wave with the corresponding amplitude. In the remainder of this section, we focus first on the parameter selection problem, which isolates the intrinsic waveform structure supported by the lattice.

4.3 Reduced Optimization Problem

Motivated by the decomposition described in the previous section, we restrict attention to the family of solitary traveling-wave solutions supported by the infinite lattice. This eliminates the explicit dependence on the input waveform $V_s(t)$ and termination R_L, and isolates the intrinsic waveform structure determined by the transmission line parameters.

We therefore consider the following reduced optimization problem: determine the parameters of the transmission line for which the associated solitary traveling-wave solution has minimal energy spread. Specifically, we seek $(\bar{c}, b)$ such that

$$\begin{aligned}
&\min_{(\bar{c},b)} && \sigma^2[\phi(\xi;\bar{c},b)] \\
&\text{subject to} && \phi(\xi-1) - 2\phi(\xi) + \phi(\xi+1) = \bar{c}^2 \frac{d^2}{d\xi^2}\big[G(\phi(\xi))\big], \\
& && \phi(\xi) \to 0 \quad \text{as } |\xi| \to \infty, \\
& && \phi(0) = 1.
\end{aligned} \tag{35}$$

Here, $\phi(\xi;\bar{c},b)$ denotes the solitary traveling-wave profile associated with parameters $(\bar{c}, b)$, and the objective $\sigma^2[\cdot]$ is the variance functional defined in Section 4.1, evaluated with respect to the normalized power density induced by $\phi(\xi)$.

The constraint $\phi(0) = 1$ fixes the nondimensional amplitude of the solution since the pulse's peak is located at $\xi = 0$ in the moving frame. As a result, the dimensional amplitude of the corresponding pulse is determined by the scaling parameter V_c, which is related to the physical parameters through

$$\bar{c} = c\sqrt{\frac{L_0 C_0}{\ell}}, \qquad b = \frac{\gamma}{V_c}. \tag{36}$$

Accordingly, for fixed physical parameters (L_0, C_0, ℓ, γ), the parameter b determines the dimensional amplitude V_c, and the optimization problem selects the amplitude of the solitary wave that minimizes the energy spread. Equivalently, for a prescribed amplitude V_c, the problem determines the effective nonlinearity parameter b and wavespeed $\bar{c}$ that produce the optimal profile.

This reduced formulation transforms the pulse synthesis problem from an optimization over inputs of a nonlinear dynamical system into a parameter selection problem for a boundary value problem. The solution of (35) characterizes the family of solitary waves with optimal concentration properties supported by the transmission line.

4.4 Finite-Domain Numerical Formulation

For numerical computation, the infinite-domain boundary value problem (35) is approximated by truncating the domain to a finite interval $[-L, L]$ and discretizing with a uniform grid. Let

$$\xi = (\xi_1, \dots, \xi_M)^\top, \qquad \xi_j = -L + (j-1)\delta, \quad j = 1, \dots, M, \tag{37}$$

where $\delta = \frac{2L}{M-1}$. The discrete waveform is represented by the vector

$$\boldsymbol{\phi} = (\phi_1, \dots, \phi_M)^\top \in \mathbb{R}^M, \qquad \phi_j \approx \phi(\xi_j). \tag{38}$$

Let $D_2 \in \mathbb{R}^{M\times M}$ denote the standard second-order finite-difference approximation of the second derivative, and let $S_+, S_- \in \mathbb{R}^{M\times M}$ denote the forward and backward shift operators, respectively. The nonlinearity is applied component-wise:

$$G(\boldsymbol{\phi}) = \big(G(\phi_1), \dots, G(\phi_M)\big)^\top. \tag{39}$$

The discrete optimization problem corresponding to (35) is then

$$\begin{aligned} \min_{(\bar{c},b)\in(1,\bar{c}_{\max}]\times(0,b_{\max}]} \quad & \sigma^2[\boldsymbol{\phi}; \bar{c}, b] \\ \text{subject to} \quad & S_-\boldsymbol{\phi} - 2\boldsymbol{\phi} + S_+\boldsymbol{\phi} = \bar{c}^2 D_2\, G(\boldsymbol{\phi}), \\ & \phi_1 = 0, \quad \phi_M = 0, \\ & \phi_{j_0} = 1, \end{aligned} \tag{40}$$

where j_0 denotes the index corresponding to the grid point closest to $\xi = 0$.

The boundary conditions $\phi_1 = \phi_M = 0$ approximate the decay condition $\phi(\xi) \to 0$ as $|\xi| \to \infty$, while the normalization $\phi_{j_0} = 1$ enforces the nondimensional amplitude constraint $\phi(0) = 1$. The truncation length L must be chosen sufficiently large so that the solution is negligible at the boundaries and truncation error does not significantly affect the objective.

For each parameter pair $(\bar{c}, b)$, the nonlinear algebraic system defined by the discrete traveling-wave equation is solved using Newton's method. Let

$$R(\boldsymbol{\phi}; \bar{c}, b) := S_-\boldsymbol{\phi} - 2\boldsymbol{\phi} + S_+\boldsymbol{\phi} - \bar{c}^2 D_2\big(G(\boldsymbol{\phi})\big), \tag{41}$$

together with the boundary and normalization constraints. A converged solution $\boldsymbol{\phi}$ defines a discrete solitary-wave profile, from which the normalized power density $p(\xi)$ and the variance σ^2 are computed.

The optimization problem (40) is solved using a grid search over the parameter space $(\bar{c}, b)$. For each parameter pair, Newton's method is initialized with a localized pulse (e.g., a sech^2 profile) and iterated until convergence. The resulting value of σ^2 is recorded, and the minimizing parameter pair is identified.

This approach is computationally intensive, as it requires solving a nonlinear system for each point in the parameter grid. However, it provides a direct characterization of the objective landscape over $(\bar{c}, b)$, which is useful for identifying the existence and structure of optimal parameter regimes.

The dominant computational cost arises from the Newton solve. The residual and Jacobian can be assembled in $O(M)$ operations due to the locality of the finite-difference and shift operators. Since the Jacobian is sparse and banded, each Newton step requires the solution of a banded linear system, with cost $O(Mw^2)$, where w is the half-bandwidth. Because the discrete shift operators represent the unit translations $\phi(\xi \pm 1)$, they shift by approximately $\lfloor 1/\delta \rfloor = \lfloor \frac{M-1}{2L} \rfloor$ grid points, so $w = O(M/L)$.

For K iterations of Newton's method per solve and a parameter grid with P^2 points, the total computational cost scales as

$$O\left(\frac{P^2 K M^3}{L^2}\right), \tag{42}$$

4.5 Large-Amplitude Traveling Waves with Optimal Energy Spread

We now present numerical results for the reduced optimization problem (40). The goals of this section are to examine the objective landscape $\sigma^2(\bar{c}, b)$ over the parameter space, identify the subset of parameter values along which the smallest sampled values of σ^2 occur, compare the corresponding traveling-wave profiles with nearby reference solutions, and assess the dimensional power spectra and peak-power characteristics of representative pulses.

We evaluate the discrete optimization problem over a finite grid in

$$(\bar{c}, b) \in (1, 2] \times (0, 2],$$

which includes both the small-amplitude regime and parameter values well beyond it. For each parameter pair, Newton's method is used to compute a candidate traveling-wave profile, and the corresponding value of the energy-spread functional σ^2 is recorded.

Figure 3 shows that the largest sampled values of $-\sigma^2$ (equivalently, the smallest sampled values of σ^2) lie along a narrow curve in parameter space. This motivates a refined numerical study of the curve

$$b = b^*(\bar{c}),$$

defined here as the collection of sampled parameter values obtained by minimizing σ^2 over b for each fixed $\bar{c}$.

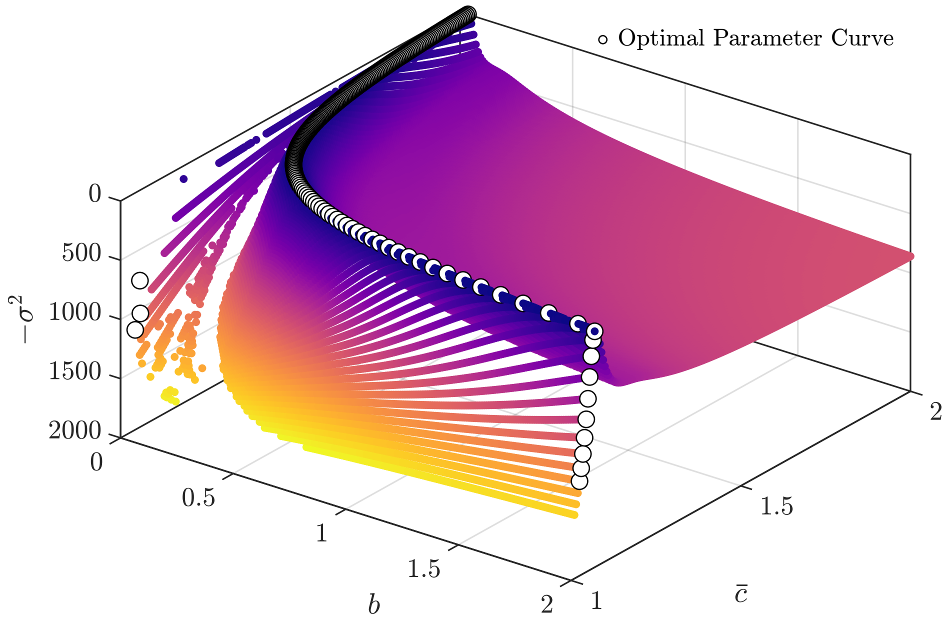

Figure 3: Energy spread $-\sigma^2$ over the parameter space $(\bar{c}, b)$. Each point corresponds to a converged numerical solution of the discretized traveling-wave problem. Note that the z-axis is $-\sigma^2$.

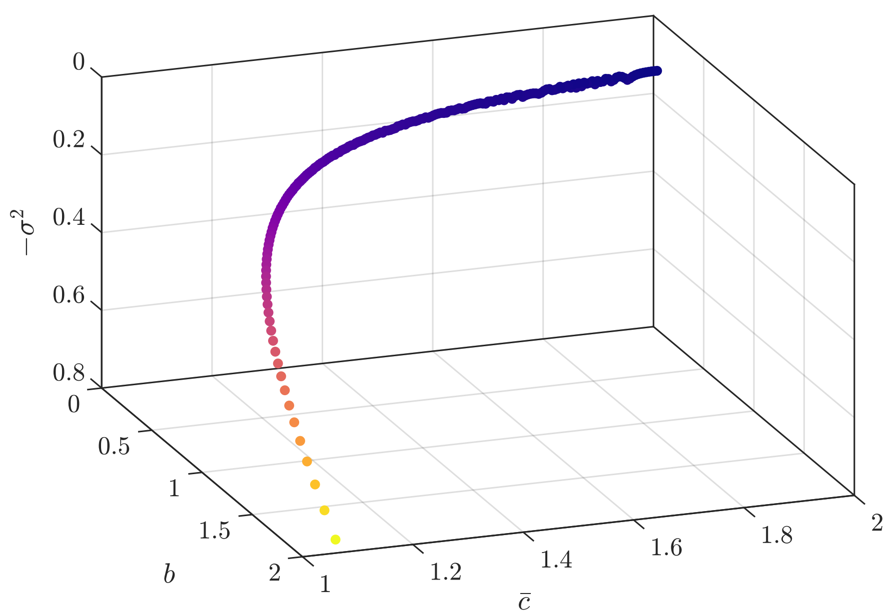

Figure 4: Numerically computed parameter curve $b = b^*(\bar{c})$ obtained by minimizing σ^2 over b for each fixed $\bar{c}$.

Figure 4 shows how the minimizing value of b varies with $\bar{c}$. Along this curve, smaller values of b correspond to larger dimensional pulse amplitudes, since

$$V_c = \frac{\gamma}{b},$$

with γ fixed. Thus, moving toward larger $\bar{c}$ along the computed curve corresponds to moving toward larger dimensional amplitudes. The numerically optimal pulse identified in this section occurs in a regime well outside $\bar{c} - 1 \ll 1$ (the optimal nondimensional wavespeed is $\bar{c}^* \approx 2$), so it is not captured by the small-amplitude KdV approximation discussed in Section 3.

We next compare traveling-wave profiles computed on and off the curve $b = b^*(\bar{c})$.

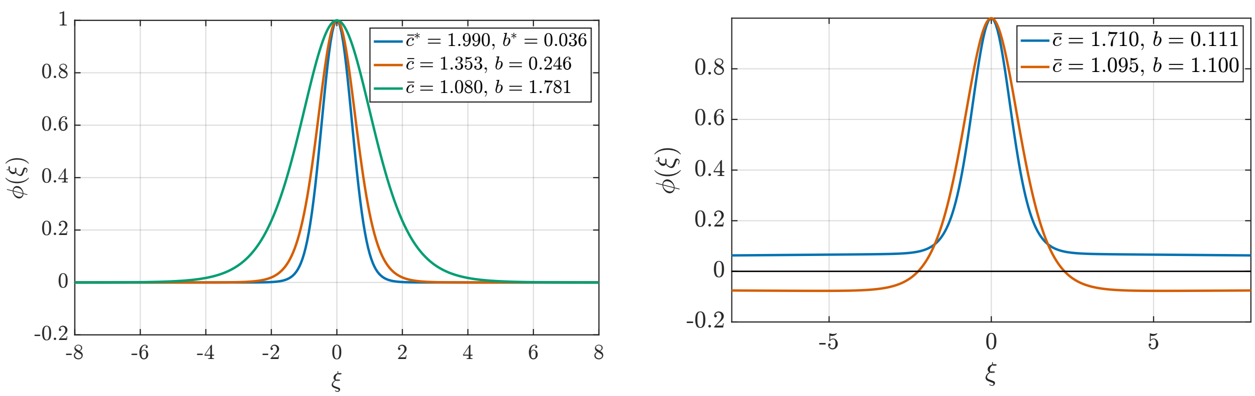

(a) Comparison of three nondimensional pulses corresponding to parameter values lying on the parameter curve $b^*(\bar{c})$.

(b) Profiles corresponding to parameter values lying below ($b < b^*(\bar{c})$) and above ($b > b^*(\bar{c})$) the computed curve $b^*(\bar{c})$.

Figure 5: Comparison of traveling-wave profiles computed on and off the curve $b = b^*(\bar{c})$. Profiles on the curve decay on both sides and become increasingly localized for larger $\bar{c}$ and smaller b. Profiles computed off the curve generally fail to exhibit decay over the computational domain.

Figure 5(a) shows that the profiles corresponding to parameter values on the computed curve are decaying and increasingly localized as one moves toward larger $\bar{c}$ and smaller b. In contrast, Figure 5(b) shows that for nearby parameter values off the curve, Newton's method often converges to profiles that do not decay across the computational domain.

Numerically, this indicates that the computed curve $b = b^*(\bar{c})$ is closely associated with the existence of strongly localized traveling-wave profiles. More precisely, among the parameter values sampled here, the parameter pairs yielding the smallest values of σ^2 are also the ones for which the computed solutions exhibit clear decay. This leads to the following numerical conjecture: decaying pulse solutions of the traveling-wave equation exist only for parameter values lying on, or very near, the approximate curve plotted in Figure 4. We leave a rigorous existence theory for these large-amplitude solitary waves as future work.

To interpret these pulses dimensionally, we fix the representative physical parameters listed in Table 2 to compute the dimensional power spectra of three representative pulses lying on the computed curve $b = b^*(\bar{c})$: the numerically optimal pulse, an intermediate-amplitude pulse, and a small-amplitude pulse.

Figure 6 shows that the large-amplitude pulse selected by the optimization exhibits substantially stronger high-frequency content than the medium- and small-amplitude reference pulses. Table 3 quantifies the corresponding values of σ^2, dimensional amplitude, peak power, and spectral centroid.

Quantity	Symbol / Expression	Value / Units
Resonant frequency	f_{res}	2 GHz
Inductance per unit cell	ℓL_0	1 nH
Capacitance per unit cell	$C_0 = \dfrac{1}{\ell L_0 (2\pi f_{\text{res}})^2}$	≈ 6.33 pF
Nonlinearity voltage scale	γ	0.8 V
Nondimensional wave speed	$\bar{c}$	obtained from optimization
Dimensional wave speed	$c = \bar{c}\sqrt{\dfrac{\ell}{L_0 C_0}}$	(derived)
Voltage scaling	$V_c = \dfrac{\gamma}{b}$	(derived)

Table 2: Dimensional parameters used for the computing physical metrics. Dimensional quantities are obtained by fixing circuit parameters and applying the scaling $V_c = \gamma/b^*$, where γ is a device parameter and b^* is determined by the optimized parameter pair $(\bar{c}^*, b^*(\bar{c}^*))$.

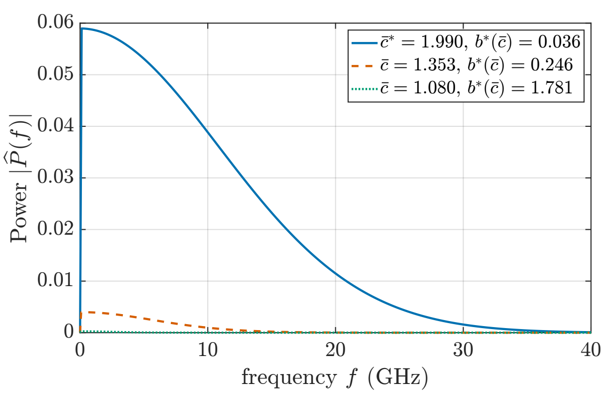

(a) Dimensional power spectra $|\widehat{P}(f)|$ for the optimal and reference pulses.

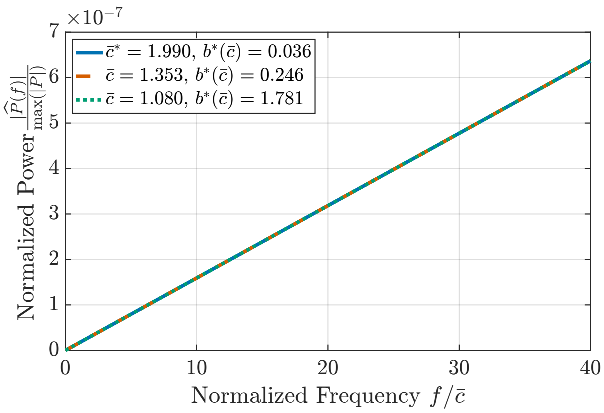

(b) Rescaled and normalized spectra, where each spectrum is divided by its maximum value and the frequency is scaled by $\bar{c}$.

Figure 6: Comparison of the spectral content of the optimal and reference pulses, all corresponding to parameter values on the curve $b = b^*(\bar{c})$.

Pulse Params	Amplitude	σ^2	Peak power	Freq. Centroid
Optimal $\bar{c}^* = 1.94,\ b^*(\bar{c}^*) = 0.041$	19.75 V	0.1360	5.4893 W	8.60 GHz
Medium $\bar{c} = 1.35,\ b^*(\bar{c}) = 0.25$	3.2041 V	0.2269	0.3397 W	4.84 GHz
Small $\bar{c} = 1.08,\ b^*(\bar{c}) = 1.772$	0.4514 V	0.7378	0.0127 W	2.22 GHz

Table 3: Comparison of energy spread, peak power, and spectral content for the pulses considered in this section.

These conclusions should be interpreted with the scope of the reduced model in mind. The optimization in this section is performed at the level of traveling-wave profiles on the infinite lattice, rather than the full finite pulse synthesizer. Accordingly, the results provide evidence that the nonlinear lattice supports a family of large-amplitude, localized solitary-wave modes. Numerically, these solitons are observed only along a one-dimensional subset of parameter space, approximated by the curve $b = b^*(\bar{c})$. Since the nondimensional speed $\bar{c}$ and the nondimensional nonlinearity strength $b = \gamma/V_c$ are both amplitude-dependent, the family of solitary waves can equivalently be parameterized by its amplitude, with $\Big(\bar{c}\big(V_c\big), b^*\big(\bar{c}(V_c)\big)\Big)$ determined implicitly along the curve.

Within the range of parameters sampled in this work, the smallest observed values of σ^2 occur along this curve.

5. Numerical Experiments of Stable Solitons

5.1 Symplectic Time Integration of the Finite Ladder

The Hamiltonian and Lagrangian of the infinite LC-ladder network are derived in Appendix D. These structures serve two purposes in this work. First, they provide the energy functional underlying the dynamics, which is essential for numerical experiments to test asymptotic stability. Since each solitary pulse has finite energy, this energy must be conserved by the dynamics for the pulse to propagate with constant profile. Thus, we use a numerical method that conserves the Hamiltonian.

Second, the Lagrangian determines an associated action functional, which provides a natural framework for studying the existence of solitary-wave solutions. In this setting, solitary waves can be characterized as critical points of the action functional. This approach has been used to establish general existence results for nonlinear lattice systems, for example by Friesecke and Wattis [25] using constrained minimization, and by Smets and Willem [26], who consider the case of prescribed wavespeed. These results do not apply directly to the present model, as the structure of the Hamiltonian differs from the settings considered in these works. However, similar variational methods may be helpful in proving the existence of solitary waves in discrete NLTLs. Extending such techniques to the large-amplitude regime considered here remains an interesting direction for future work.

The Hamiltonian for the infinite lattice can be adapted to a finite lattice with nodes $n = 1, \ldots, N$. On a finite interval away from the boundaries, or equivalently for time intervals after the pulse is injected and prior to its interaction with the boundary termination, the interior lattice dynamics are governed by the Hamiltonian,

$$\mathcal{H}(\boldsymbol{\Phi}, \boldsymbol{Q}) = \sum_{n=1}^{N} \Psi(Q_n) + \sum_{n=1}^{N-1} \frac{1}{2\ell L_0} \big(\Phi_n - \Phi_{n+1}\big)^2, \tag{43}$$

where (Φ_n, Q_n) form a canonical pair and $\Psi(Q_n)$ is defined in Appendix D. Hamilton's equations yield

$$\dot{\Phi}_n = V(Q_n), \tag{44}$$

$$\dot{Q}_n = \frac{1}{\ell L_0} \left(\Phi_{n-1} - 2\Phi_n + \Phi_{n+1}\right), \tag{45}$$

for interior nodes $n = 2, \ldots, N-1$, where $V(Q_n)$ denotes the inverse constitutive relation defined by $Q_n = C_0 G(V_n)$.

The Hamiltonian is separable,

$$H(\Phi, Q) = T(Q) + U(\Phi),$$

with

$$T(Q) = \sum_{n=1}^{N} \Psi(Q_n), \qquad U(\Phi) = \sum_{n=1}^{N-1} \frac{1}{2\ell L_0} (\Phi_n - \Phi_{n+1})^2.$$

This separable structure permits the use of the Störmer–Verlet method, an explicit symplectic integration scheme. In the absence of forcing and dissipation, the method preserves a modified Hamiltonian that differs from the true Hamiltonian by $O(\Delta t^2)$ [27].

Störmer–Verlet scheme. Time is discretized with timestep Δt. We employ a staggered update in which currents are evaluated at half time steps and charges at integer time steps.

Current update (half step):

$$I_n^{k+\frac{1}{2}} = I_n^{k-\frac{1}{2}} + \Delta t \, \frac{V_n^k - V_{n+1}^k}{\ell L_0}, \qquad n = 1, \ldots, N-1. \tag{46}$$

Charge update (full step):

$$Q_n^{k+1} = Q_n^k + \Delta t \left(I_{n-1}^{k+\frac{1}{2}} - I_n^{k+\frac{1}{2}} \right), \qquad n = 2, \ldots, N-1. \tag{47}$$

The voltage is recovered pointwise from the constitutive relation

$$Q_n^k = C_0 G(V_n^k), \qquad V_n^k = V(Q_n^k),$$

Boundary conditions. The forcing and load are incorporated directly into the updates. At the left boundary, the injected waveform is imposed through

$$Q_1^{k+1} = Q\big(V_s^{k+1}\big), \tag{48}$$

which enforces the prescribed source voltage.

At the right boundary, the resistive load introduces dissipation through

$$Q_{N+1}^{k+1} = Q_{N+1}^k + \Delta t \left(I_N^{k+\frac{1}{2}} - \frac{V_{N+1}^k}{R_L} \right). \tag{49}$$

Because the right boundary uses a constant resistance R_L, it cannot be perfectly matched to the propagating waveform and therefore introduces dissipation. As a result, the finite-lattice dynamics are no longer Hamiltonian once the pulse interacts with the termination, and the symplectic structure of the scheme is no longer relevant to the physical system being simulated.

To isolate the intrinsic dynamics of the lattice and assess stability of the solitary waves under conservative evolution, we restrict all simulations to time intervals for which the pulse remains well-separated from the right boundary. In practice, this corresponds to terminating the simulation before the leading edge of the pulse reaches the final unit cell.

The integration scheme used has another advantage of being efficient. Each timestep requires only nearest-neighbor differences and pointwise evaluation of the nonlinear constitutive relation. Therefore, the computational cost per timestep scales linearly with the number of unit cells, $O(N)$, and a simulation over T timesteps requires $O(TN)$ operations.

5.1.1 Experiment I: Injection of the Optimized Soliton Mode

The first numerical experiment tests whether the optimized traveling-wave solution remains stable under the full finite-lattice dynamics. Specifically, we use the numerically optimal solitary-wave profile computed in Section 4.5 as the injected waveform and evolve it using the symplectic scheme described in Section 5.1.

We use $N = 200$ unit cells total and simulate in the nondimensional time variable τ.

The injected voltage is defined by mapping the traveling-wave profile $\phi(\xi)$ into the time domain via

$$\frac{V_s(\tau)}{V_c} = \phi_s(\tau) = \phi^*(-\bar{c}\tau), \tag{50}$$

where $\phi^*(\xi)$ is the optimal profile found in section 4.5 for $\bar{c}^* \approx 1.99$ and $b^* \approx 0.036$, so that the waveform enters the lattice with the correct amplitude and propagation speed.

The purpose of this experiment is to assess whether the solitary wave is a dynamically stable traveling-wave solution, i.e., whether it propagates with approximately constant shape and amplitude over long time intervals in the absence of boundary interaction.

As discussed in Section 5.1, the right boundary introduces dissipation through the load R_L. To isolate the intrinsic dynamics of the lattice, all simulations are terminated after reaching the 175$^{\text{th}}$ unit cell, before the pulse reaches the right boundary.

We evaluate stability by comparing the injected waveform $V_s(\tau)$ with the waveform measured at downstream lattice sites, the evolution of the pulse shape as it propagates through the lattice, and the peak amplitude and temporal width of the pulse over time.

Figure 7 shows the evolution of the voltage waveform at several lattice sites. A stable solitary wave is characterized by translation of the pulse without significant change in shape.

Figure 8 shows the injected nondimensional waveform $\phi_s(\tau)$ compared to the nondimensional voltage $\phi_{150}(\tau)$ measured at the 150$^{\text{th}}$ unit cell on the NLTL. Agreement between these profiles indicates that the pulse propagates without significant distortion.

These results provide numerical evidence that the optimized traveling-wave solution corresponds

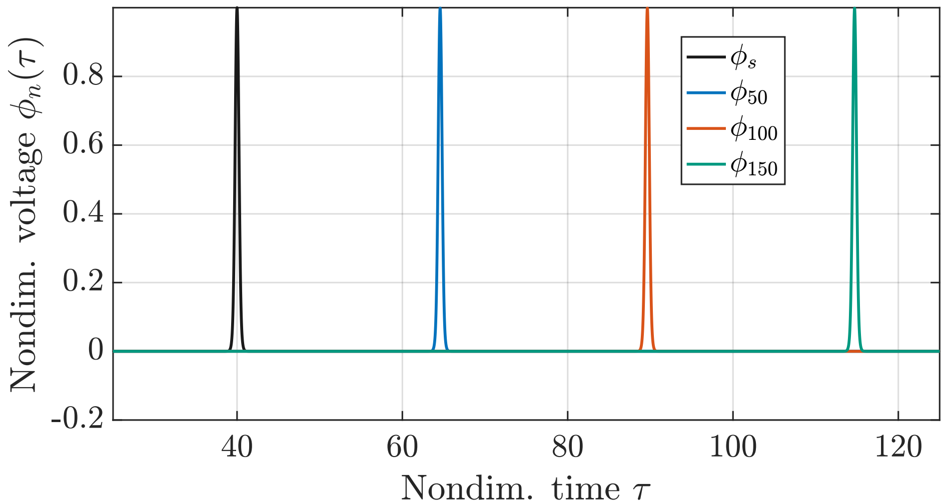

Figure 7: Propagation of the optimized soliton mode under the nondimensional finite-lattice dynamics at several lattice sites prior to boundary interaction.

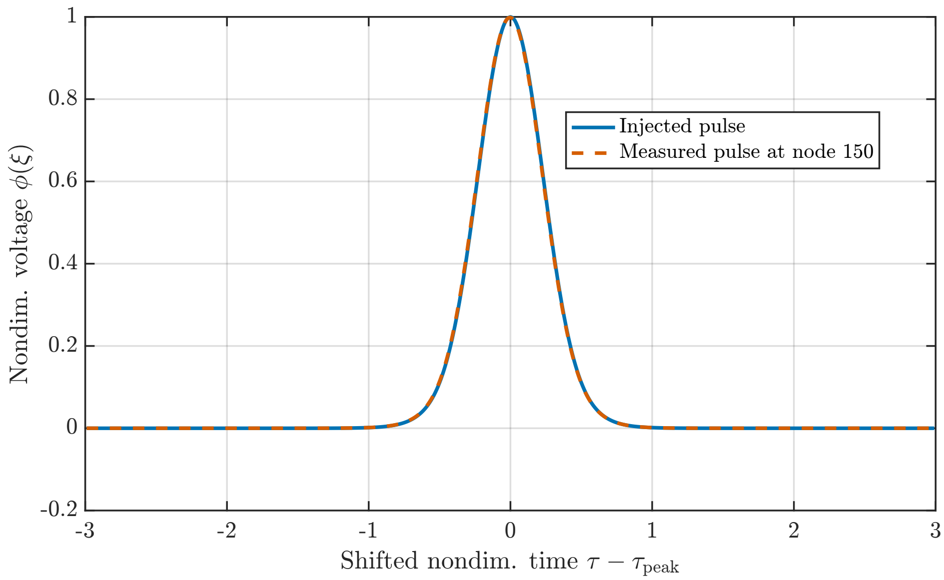

Figure 8: Comparison between nondimensional injected waveform and the nondimensional waveform measured at the 150$^{\text{th}}$ unit cell. Shifted by τ_{peak}, the nondimensional time at which the pulse's peak was recorded.

to a dynamically stable solitary wave of the lattice system.

5.1.2 Experiment II: Propagation of a Trapezoidal Input Pulse

The second experiment examines the evolution of a physically realizable, non-soliton input waveform under the nonlinear lattice dynamics. Unlike the previous experiment, which injects an exact solitary-wave profile, the objective here is to determine whether the system dynamically organizes a generic input into a sequence of solitary waves with amplitude-dependent propagation speeds, similar to the behavior observed in the KdV equation. This experiment also illustrates the use of NLTLs for pulse synthesis. Following [10], a trapezoidal input pulse with large width and relatively low peak amplitude is used, and its evolution into a sequence of shorter, higher-amplitude pulses is examined.

The injected waveform is taken to be a trapezoidal pulse with controllable amplitude, rise time, and pulse width. These parameters are chosen so that the width of the input is approximately 10 times larger than that of the solitary wave supported by the optimized parameters $(\bar{c}, b) = (1.990, 0.036)$, for which the corresponding solitary wave has nondimensional amplitude $\|\phi(-\bar{c}\tau)\|_\infty = 1$. This ensures that the initial waveform is significantly broader than a solitary-wave solution.

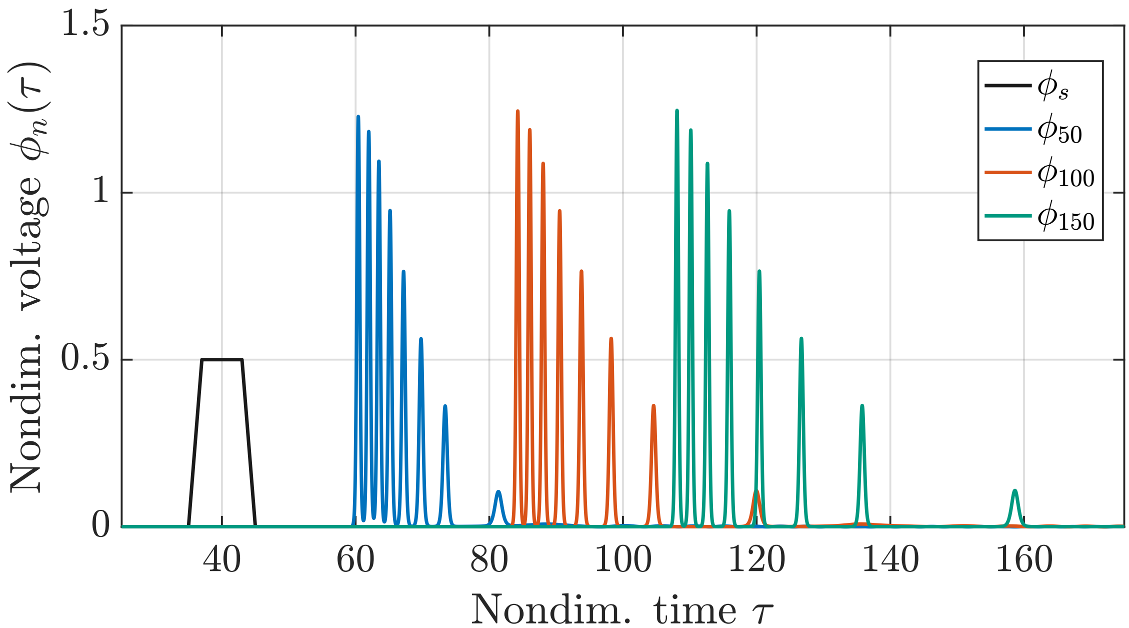

Figure 9: Propagation of a trapezoidal input waveform measured at the input (ϕ_s), 50$^{\text{th}}$ (ϕ_{50}), 100$^{\text{th}}$ (ϕ_{100}), and 150$^{\text{th}}$ (ϕ_{150}) unit cells respectively. The initial smooth pulse steepens and separates into stable solitons with amplitude-dependent speeds as it propagates through the NLTL.

Figure 9 shows the voltage waveform measured at several lattice sites. The initially smooth trapezoidal pulse undergoes nonlinear steepening and subsequently decomposes into a sequence of localized pulses. These pulses propagate at different speeds, with larger-amplitude pulses traveling faster. This qualitative behavior is consistent with the KdV equation, where wave speed increases with amplitude.

A nondimensional amplitude of 1 corresponds to the optimized parameters $(\bar{c}, b) = (1.99, 0.036)$, for which $\bar{c} - 1 \approx 1$ and $1/b \approx 27.8$. The small-amplitude regime applies when $\bar{c} - 1 \ll 1$ and $1/b \ll 1$, so the largest pulses shown in Figure 9 lie well outside the small-amplitude regime.

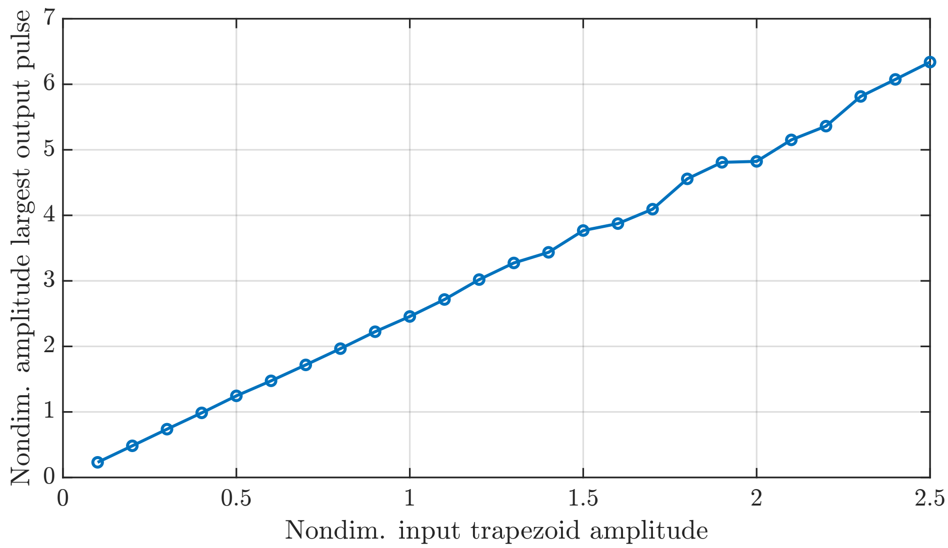

Figure 10: Relationship between input trapezoidal amplitude and the amplitude of the largest output soliton pulse.

It is also desirable for NLTLs to support flexible pulse compression in applications [1]. The width of the largest output pulse is determined by its amplitude. To quantify this relationship, we vary the amplitude of the injected trapezoidal pulse while keeping the width and rise time fixed, and record the nondimensional amplitude of the largest resulting solitary pulse. The amplitude is measured from the peak value of the leading pulse (the largest and fastest pulse) observed at the 150^{th} unit cell.

The results, shown in Figure 10, demonstrate that the amplitude of the leading output pulse depends approximately linearly on the input amplitude. For sufficiently long lines, the largest-amplitude pulse consistently emerges first, followed by smaller trailing pulses. This ordering reflects the amplitude–speed relationship observed in Figure 9.

These results show that, for the parameter regime considered here, the nonlinear lattice dynamics transform a broad input waveform into a collection of localized traveling pulses whose amplitudes and speeds are determined by the input. The leading pulse is consistent with the solitary-wave solutions computed for the infinite lattice, indicating that the reduced optimization problem in Section 4 captures the dominant structures observed in the full finite-lattice dynamics.

5.2 Circuit-Level Validation in a Commercial Solver

In this section, we repeat the two experiments of Section 5.1 using a dimensional circuit model implemented in a commercial circuit simulator (Keysight ADS). The purpose of this section is to verify that the nondimensional results from the Störmer Verlet integration method agree with those of a commercial solver.

All simulations in this section are performed using the dimensional parameters listed in Table 2. The nondimensional traveling-wave profiles computed in Section 4 are converted to dimensional waveforms using the relations

$$V = V_c \phi, \qquad t = \frac{\sqrt{\ell L_0 C_0}}{\bar{c}} \xi,$$

where $V_c = \gamma/b$ and $(\bar{c}, b) = (1.99, 0.036)$ are the optimized parameters. These dimensional waveforms are then used as inputs to the circuit model.

We first inject the optimized solitary-wave profile corresponding to $(\bar{c}, b) = (1.990, 0.036)$ into the dimensional circuit model. The injected waveform is obtained by mapping the nondimensional profile $\phi(\xi)$ into the time domain using the scaling above.

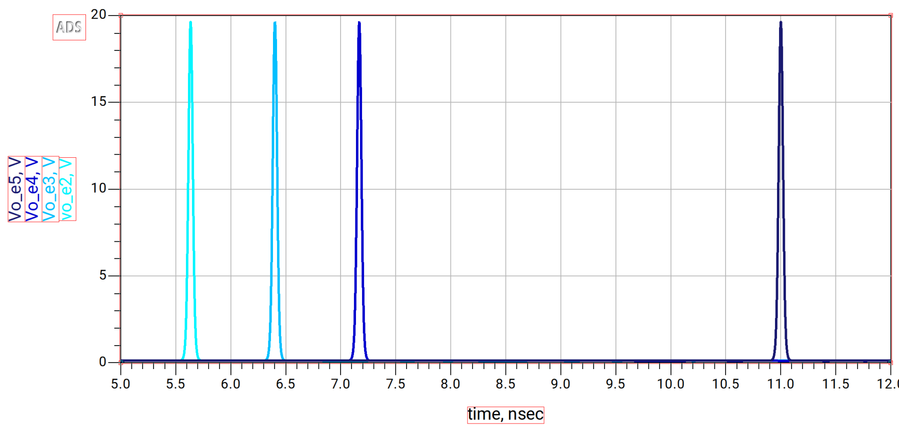

Figure 11: Comparison of the injected dimensional soliton waveform and the waveform measured at a downstream node in the ADS simulation.

Figure 11 shows the injected waveform and the waveform measured at a downstream node. The pulse propagates with minimal distortion, maintaining its shape and amplitude over the simulated time interval prior to boundary interaction. This is consistent with the behavior observed in Section 5.1 and indicates that the optimized traveling-wave solution corresponds to a robust propagating pulse in the dimensional circuit model.

We next consider the evolution of a dimensional trapezoidal input pulse with fixed amplitude, rise time, and width. The parameters are chosen to match those used in Section 5.1 after dimensional scaling.

Figure 12 shows the waveform measured at several nodes along the transmission line. As in the nondimensional simulations, the initial trapezoidal pulse undergoes nonlinear steepening and decomposes into a sequence of localized pulses. The leading pulse has the largest amplitude and propagates at the highest speed, followed by smaller trailing pulses.

This behavior is consistent with the results of Section 5.1 and demonstrates that the qualitative features of pulse decomposition and amplitude-dependent propagation persist in the dimensional circuit model. In particular, the leading pulse is consistent with the solitary-wave solutions computed from the infinite lattice model.

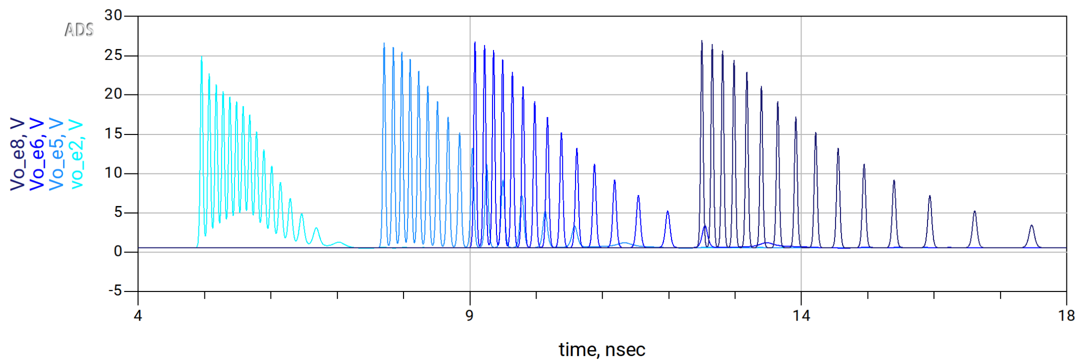

Figure 12: Propagation of a dimensional trapezoidal input waveform measured every 25 unit cells in the commercial circuit simulation.

Taken together, these results show that the dynamics observed in the nondimensional model are reproduced in a physically parameterized circuit simulation using an independent numerical solver. This provides additional evidence that the solitary-wave structures identified in Section 4 are relevant for practical pulse synthesis in nonlinear transmission lines.

6. Conclusion

This work develops a computational framework for the design of nonlinear transmission lines (NLTLs) that support short, high-power soliton pulses beyond the classical small-amplitude regime. Starting from the discrete LC-ladder model, we derived the reduced dynamics governing the profile of soliton solutions and posed pulse synthesis as an optimization problem over these solutions. By introducing a physically motivated objective based on the variance of the normalized power distribution, we identified parameter regimes that yield highly localized, large-amplitude soliton pulses.

Numerically, we demonstrated that the discrete lattice supports a family of strongly localized traveling-wave solutions that are not captured by the continuum approximation. These solutions appear to lie along a curve in parameter space, along which the energy-spread functional is minimized. Time-domain simulations of the full finite lattice show that these profiles propagate with minimal distortion over long distances prior to boundary interaction. In addition, generic input waveforms were observed to evolve into trains of localized pulses with amplitude-dependent speeds, which provides evidence for the asymptotic stability of large-amplitude solitons. These results were further validated using a dimensional circuit model in a commercial solver, confirming that the predicted dynamics persist for an alternative numerical method.

From a theoretical perspective, we view this work as a first step toward extending the analytical framework of soliton theory, which is well-developed for continuum models such as the KdV equation, to discrete nonlinear lattice systems. A central open problem is the rigorous proof of existence and stability of large-amplitude traveling-wave solutions for the discrete lattice equation considered here. While related variational techniques exist in the literature for other lattice models [25, 26], extending these results to the present setting remains an important direction for future work.

Several additional avenues for future research arise from this study. First, experimental validation of the predicted soliton dynamics using a physical LC-ladder network is currently underway, and will be essential for assessing the practical relevance of the proposed design framework. Second, the analysis here is restricted to a simple LC-ladder topology with nonlinear capacitors. Extending these methods to more general NLTL architectures, including those with nonlinear inductors or more complex topologies, is a natural next step.

Another key challenge is the boundary termination problem. Efficient extraction of large-amplitude pulses requires boundary conditions that approximate transparent (non-reflecting) behavior, which are inherently nonlocal in time for nonlinear systems. Developing physically realizable approximations of such boundary conditions with standard circuit components remains an open and practically important problem.

Finally, the design of the input waveform constitutes a nonlinear inverse problem. In this work, we briefly examine this through trapezoidal inputs and observe a continuous relationship between the input amplitude and the amplitude of the resulting soliton. However, a general framework for selecting input waveforms that reliably generate a desired soliton profile is not developed here. Establishing such a framework remains an important direction for future work.

Overall, the results presented here provide both numerical evidence and a conceptual framework for understanding large-amplitude soliton formation in discrete nonlinear electrical networks. Our results show that principled, model-based design of NLTL pulse synthesizers is feasible beyond the classical small-amplitude regime.

References

[1] M. Rahman and K. Wu, "A nonlinear transmission line technique for generating efficient and low-ringing picosecond pulses for ultrabroadband and ultrafast systems," *IEEE Transactions on Instrumentation and Measurement*, vol. 71, pp. 1–11, 2022.

[2] J. Benford, J. A. Swegle, and E. Schamiloglu, *High Power Microwaves*. Boca Raton, FL: CRC Press, 3rd ed., 2016.

[3] M. Hussain, "Ultra-wideband impulse radar-an overview of the principles," *IEEE Aerospace and Electronic Systems Magazine*, vol. 13, no. 9, pp. 9–14, 1998.

[4] J. D. Taylor, ed., *Introduction to Ultra-Wideband Radar Systems*. CRC Press, 1 ed., 1994.

[5] S. Hagness, A. Taflove, and J. Bridges, "Two-dimensional fdtd analysis of a pulsed microwave confocal system for breast cancer detection: fixed-focus and antenna-array sensors," *IEEE Transactions on Biomedical Engineering*, vol. 45, no. 12, pp. 1470–1479, 1998.

[6] S. Gezici, Z. Tian, G. Giannakis, H. Kobayashi, A. Molisch, H. Poor, and Z. Sahinoglu, "Localization via ultra-wideband radios: a look at positioning aspects for future sensor networks," *IEEE Signal Processing Magazine*, vol. 22, no. 4, pp. 70–84, 2005.

[7] J. D. C. Darling and P. W. Smith, "High-power pulsed rf extraction from nonlinear lumped element transmission lines," *IEEE Transactions on Plasma Science*, vol. 36, no. 5, pp. 2598–2603, 2008.

[8] B. Seddon, C. R. Spikings, and J. E. Dolan, "Rf pulse formation in nonlinear transmission lines," in *Proceedings of the 16th IEEE International Pulsed Power Conference (PPC)*, pp. 678–681, IEEE, 2007.

[9] M. Brown and P. Smith, "High power, pulsed soliton generation at radio and microwave frequencies," in *Digest of Technical Papers. 11th IEEE Int. PPC*, vol. 1, pp. 346–354 vol.1, 1997.

[10] N. Kuek, A. Liew, E. Schamiloglu, and J. Rossi, "Circuit modeling of nonlinear lumped element transmission lines," in *2011 IEEE Pulsed Power Conference*, pp. 185–192, 2011.

[11] N. S. Kuek, A. C. Liew, E. Schamiloglu, and J. O. Rossi, "Pulsed rf oscillations on a nonlinear capacitive transmission line," *IEEE Transactions on Dielectrics and Electrical Insulation*, vol. 20, no. 4, pp. 1129–1135, 2013.

[12] C. Spikings, N. Seddon, R. Ibbotson, and J. Dolan, "Hpm systems based on nltl technologies," in *2009 IET Conference on High Power RF Technologies*, pp. 1–3, 2009.

[13] E. Afshari and A. Hajimiri, "Nonlinear transmission lines for pulse shaping in silicon," *IEEE Journal of Solid-State Circuits*, vol. 40, no. 3, pp. 744–752, 2005.

[14] M. Turner, G. Branch, and P. Smith, "Methods of theoretical analysis and computer modeling of the shaping of electrical pulses by nonlinear transmission lines and lumped-element delay lines," *IEEE Transactions on Electron Devices*, vol. 38, no. 4, pp. 810–816, 1991.

[15] M. Remoissenet, *Waves Called Solitons: Concepts and Experiments*. Advanced Texts in Physics, Springer Berlin Heidelberg, 3 ed., 1999.

[16] M. Samizadeh Nikoo, S. M.-A. Hashemi, and F. Farzaneh, "Theory of rf pulse generation through nonlinear transmission lines," *IEEE Transactions on Microwave Theory and Techniques*, vol. 66, no. 7, pp. 3234–3244, 2018.

[17] R. L. Pego and M. I. Weinstein, "Asymptotic stability of solitary waves," *Communications in Mathematical Physics*, vol. 164, no. 2, pp. 305–349, 1994.

[18] M. J. Ablowitz and H. Segur, "Asymptotic solutions of the korteweg-devries equation," *Studies in Applied Mathematics*, vol. 57, no. 1, pp. 13–44, 1977.

[19] P. C. Schuur, *The emergence of solitons of the Korteweg-de Vries equation from arbitrary initial conditions*, pp. 13–33. Berlin, Heidelberg: Springer Berlin Heidelberg, 1986.

[20] J. Johnson and C. Scarborough, "Iterative technique for computing soliton solutions to periodic nonlinear electrical networks," *Optical Materials Express*, vol. 14, pp. 649–663, 2024.

[21] M. Samizadeh Nikoo and S. M.-A. Hashemi, "New soliton solution of a varactor-loaded nonlinear transmission line," *IEEE Transactions on Microwave Theory and Techniques*, vol. 65, no. 11, pp. 4084–4092, 2017.

[22] S. M. Sze and K. K. Ng, *Physics of Semiconductor Devices*. Hoboken, NJ: John Wiley & Sons, 3rd ed., 2006.

[23] M. Ehrhardt, "Discrete transparent boundary conditions for schrödinger-type equations for non-compactly supported initial data," *Applied Numerical Mathematics*, vol. 58, no. 5, pp. 660–673, 2008.

[24] M. Samizadeh Nikoo, S. M.-A. Hashemi, and F. Farzaneh, "Theory of terminated nonlinear transmission lines," *IEEE Transactions on Microwave Theory and Techniques*, vol. 66, no. 1, pp. 91–99, 2018.

[25] G. Friesecke and J. A. D. Wattis, "Existence theorem for solitary waves on lattices," *Communications in Mathematical Physics*, vol. 161, no. 2, pp. 391–418, 1994.

[26] D. Smets and M. Willem, "Solitary waves with prescribed speed on infinite lattices," *Journal of Functional Analysis*, vol. 149, no. 1, pp. 266–275, 1997.

[27] E. Hairer, C. Lubich, and G. Wanner, *Geometric numerical integration illustrated by the Störmer–Verlet method*, p. 399–450. Acta Numerica, Cambridge University Press, 2003.

A. Derivation of the KdV Approximation from the Discrete Lattice Dynamics

We begin with the discrete lattice equation

$$V_{n-1}(t) - 2V_n(t) + V_{n+1}(t) = \ell L_0 C_0 \frac{d^2}{dt^2}\left[G\big(V_n(t)\big)\right], \tag{51}$$

where $n \in \mathbb{Z}$ indexes the unit cells, ℓ is the cell length, and F is the nondimensional nonlinear capacitance law.

Our goal in this appendix is not to derive a traveling-wave equation, but rather a weakly nonlinear, weakly dispersive *evolution equation* that approximates the lattice dynamics (51) in the long-wavelength, small-amplitude regime. The resulting reduced model is the Korteweg–de Vries (KdV) equation. This follows the reductive perturbation approach presented by Remoissenet [15] for nonlinear transmission lines, adapted here to the present lattice model.

Since $V_n(t)$ is defined only at integer lattice sites, we introduce a smooth (analytic) interpolating field $V(x,t)$ on $\mathbb{R} \times \mathbb{R}_+$ such that

$$V_n(t) = V(n\ell, t). \tag{52}$$

Expanding about the point $x = n\ell$ gives

$$V(x \pm \ell, t) = V(x,t) \pm \ell V_x(x,t) + \frac{\ell^2}{2} V_{xx}(x,t) \pm \frac{\ell^3}{6} V_{xxx}(x,t) + \frac{\ell^4}{24} V_{xxxx}(x,t) + O(\ell^5). \tag{53}$$

Hence

$$V(x-\ell,t) - 2V(x,t) + V(x+\ell,t) = \ell^2 V_{xx} + \frac{\ell^4}{12} V_{xxxx} + O(\ell^6 \partial_x^6 V). \tag{54}$$

Substituting (54) into (51) yields

$$\ell^2 V_{xx} + \frac{\ell^4}{12} V_{xxxx} + O(\ell^6 \partial_x^6 V) = \ell L_0 C_0 \, \partial_t^2 \left[G(V)\right]. \tag{55}$$

A.1 Weakly nonlinear regime

To obtain a KdV approximation, we assume the pulse amplitude is small. Accordingly, we expand the nonlinear capacitance law about $V = 0$:

$$F(V) = 1 - \alpha V + O\Big(\frac{V^2}{\gamma^2}\Big), \qquad \alpha := -F'(0). \tag{56}$$

For the varactor law

$$F(V) = \left(1 + \frac{V}{\gamma}\right)^{-m}, \tag{57}$$

one has

$$\alpha = \frac{m}{\gamma}. \tag{58}$$

Using (56),

$$G(V) = \int_0^V F(s)\, ds = V - \frac{\alpha}{2} V^2 + O(V^3). \tag{59}$$

Therefore (55) becomes

$$\ell^2 V_{xx} + \frac{\ell^4}{12} V_{xxxx} = \ell L_0 C_0\, \partial_t^2 \Big(V - \frac{\alpha}{2} V^2\Big) + O\Big(\ell^6 \partial_x^6 V\Big) + O\Big(\partial_t^2 V^3\Big). \tag{60}$$

Dividing by $\ell L_0 C_0$ and introducing the linear long-wave speed

$$c_0^2 := \frac{\ell}{L_0 C_0}, \tag{61}$$

we obtain

$$\partial_t^2 \Big(V - \frac{\alpha}{2} V^2\Big) = c_0^2 V_{xx} + \frac{c_0^2 \ell^2}{12} V_{xxxx} + O\Big(\ell^4 \partial_x^6 V\Big) + O\Big(\partial_t^2 V^3\Big). \tag{62}$$

Equivalently,

$$V_{tt} - c_0^2 V_{xx} = \frac{\alpha}{2} (V^2)_{tt} + \frac{c_0^2 \ell^2}{12} V_{xxxx} + \cdots. \tag{63}$$

We now look for weakly nonlinear, long waves traveling predominantly to the right with speed close to c_0. Following the standard reductive perturbation method, we introduce the slow variables

$$X = \varepsilon^{1/2} \frac{x - c_0 t}{\ell}, \qquad T = \varepsilon^{3/2} \frac{c_0 t}{\ell}, \qquad 0 < \varepsilon \ll 1, \tag{64}$$

and seek a solution of the form

$$V(x,t) = \varepsilon U(X,T) + \varepsilon^2 U_2(X,T) + \cdots. \tag{65}$$

The derivative operators become

$$\partial_x = \frac{\varepsilon^{1/2}}{\ell} \partial_X, \qquad \partial_t = -\frac{c_0 \varepsilon^{1/2}}{\ell} \partial_X + \frac{c_0 \varepsilon^{3/2}}{\ell} \partial_T. \tag{66}$$

Hence

$$V_{xx} = \frac{\varepsilon^2}{\ell^2}U_{XX} + O(\varepsilon^3), \tag{67}$$

$$V_{xxxx} = \frac{\varepsilon^3}{\ell^4}U_{XXXX} + O(\varepsilon^4), \tag{68}$$

$$V_{tt} = \frac{c_0^2}{\ell^2}\left(\varepsilon^2 U_{XX} - 2\varepsilon^3 U_{XT} + O(\varepsilon^4)\right), \tag{69}$$

$$(V^2)_{tt} = \frac{c_0^2}{\ell^2}\left(\varepsilon^3 (U^2)_{XX} + O(\varepsilon^4)\right). \tag{70}$$

Substituting these expressions into (63) and collecting terms gives:

At order $O(\varepsilon^2)$,

$$\frac{c_0^2}{\ell^2}U_{XX} - \frac{c_0^2}{\ell^2}U_{XX} = 0, \tag{71}$$

so the leading linear transport at speed c_0 is automatically satisfied.

At order $O(\varepsilon^3)$, we obtain

$$-2U_{XT} = \frac{\alpha}{2}(U^2)_{XX} + \frac{1}{12}U_{XXXX}. \tag{72}$$

Assuming U and its derivatives decay as $|X| \to \infty$, we integrate once with respect to X to obtain

$$-2U_T = \frac{\alpha}{2}(U^2)_X + \frac{1}{12}U_{XXX}. \tag{73}$$

Using $(U^2)_X = 2UU_X$, this becomes

$$U_T + \frac{\alpha}{2}UU_X + \frac{1}{24}U_{XXX} = 0. \tag{74}$$

Equation (74) is the KdV equation governing the leading-order, right-moving, small-amplitude dynamics of the discrete lattice (51) in the long-wavelength limit.

B. Derivation of the Solitary-Wave Solution of the KdV Equation

We seek a positive localized traveling-wave solution of

$$U_T + \frac{\alpha}{2}UU_X + \frac{1}{24}U_{XXX} = 0 \tag{75}$$

in the form

$$U(X,T) = W(\zeta), \qquad \zeta = X - \lambda T, \tag{76}$$

where $\lambda > 0$ is the dimensionless wave speed in the slow variables. Substituting gives

$$-\lambda W_\zeta + \frac{\alpha}{2}WW_\zeta + \frac{1}{24}W_{\zeta\zeta\zeta} = 0. \tag{77}$$

Assuming $W(\zeta) \to 0$ and its derivatives vanish as $|\zeta| \to \infty$, we integrate once with respect to ζ to obtain

$$-\lambda W + \frac{\alpha}{4}W^2 + \frac{1}{24}W_{\zeta\zeta} = 0, \tag{78}$$

or equivalently,

$$W_{\zeta\zeta} = 24\lambda W - 6\alpha W^2. \tag{79}$$

We now seek a positive, localized solution of (79) in the form

$$W(\zeta) = A\,\mathrm{sech}^2(B\zeta), \tag{80}$$

where $A > 0$ and $B > 0$ are constants to be determined. Using

$$\frac{d^2}{d\zeta^2}\mathrm{sech}^2(B\zeta) = 4B^2\mathrm{sech}^2(B\zeta) - 6B^2\mathrm{sech}^4(B\zeta), \tag{81}$$

we find

$$W_{\zeta\zeta} = 4B^2W - \frac{6B^2}{A}W^2. \tag{82}$$

Comparing this expression with (79) yields

$$4B^2 = 24\lambda, \qquad \frac{6B^2}{A} = 6\alpha. \tag{83}$$

Therefore,

$$B^2 = 6\lambda, \qquad A = \frac{6\lambda}{\alpha}. \tag{84}$$

Hence the solitary-wave solution of the KdV equation is

$$U(X,T) = \frac{6\lambda}{\alpha}\,\mathrm{sech}^2\big(\sqrt{6\lambda}\,(X - \lambda T)\big). \tag{85}$$

Recalling the slow variables

$$X = \varepsilon^{1/2}\frac{x - c_0 t}{\ell}, \qquad T = \varepsilon^{3/2}\frac{c_0 t}{\ell}, \tag{86}$$

the corresponding dimensional pulse travels with speed

$$c = c_0(1 + \varepsilon\lambda), \tag{87}$$

and has leading-order form

$$V(x,t) \approx \varepsilon\frac{6\lambda}{\alpha}\,\mathrm{sech}^2\left[\frac{\varepsilon^{1/2}\sqrt{6\lambda}}{\ell}\big(x - c_0(1+\varepsilon\lambda)t\big)\right]. \tag{88}$$

C. Newton's Method Implementation

To solve the discrete constrained optimization problem numerically, we first define the nonlinear residual corresponding to the discretized traveling-wave equation. Let $\boldsymbol{\xi}$ be a discretization of ξ from $[-L, L]$ with uniform step-size δ chosen so that $\frac{2L}{\delta}, \frac{1}{\delta} \in \mathbb{Z}$. Then, let

$$\bar{m} = \frac{1}{\delta} \tag{89}$$

so that a unit shift in the traveling coordinate corresponds to a shift of $\bar{m}$ grid points. The forward and backward shift operators $S_+, S_- \in \mathbb{R}^{M\times M}$ are defined by

$$(S_+)_{ij} = \begin{cases} 1, & j = i + \bar{m}, \\ 0, & \text{otherwise}, \end{cases} \tag{90}$$

$$(S_-)_{ij} = \begin{cases} 1, & j = i - \bar{m}, \\ 0, & \text{otherwise}. \end{cases} \tag{91}$$

Equivalently,

$$S_+\boldsymbol{\phi} = (\phi_{1+\bar{m}}, \dots, \phi_M, 0, \dots, 0)^\top, \tag{92}$$

$$S_-\boldsymbol{\phi} = (0, \dots, 0, \phi_1, \dots, \phi_{M-\bar{m}})^\top. \tag{93}$$

Define the componentwise map

$$\boldsymbol{G}(\boldsymbol{\phi}) = \big(G(\phi_1), \dots, G(\phi_M)\big)^\top. \tag{94}$$

Then the unconstrained residual is

$$\boldsymbol{R}_0(\boldsymbol{\phi}; \bar{c}, b) = S_-\boldsymbol{\phi} - 2\boldsymbol{\phi} + S_+\boldsymbol{\phi} - \bar{c}^2 D_2 \boldsymbol{G}(\boldsymbol{\phi}; b). \tag{95}$$

To enforce decay at the truncated boundaries and the amplitude normalization, we replace three rows of the residual:

$$R_1(\boldsymbol{\phi}; \bar{c}, b) = \phi_1, \tag{96}$$

$$R_M(\boldsymbol{\phi}; \bar{c}, b) = \phi_M, \tag{97}$$

$$R_{j_0}(\boldsymbol{\phi}; \bar{c}, b) = \phi_{j_0} - A^*, \tag{98}$$

where j_0 is the index corresponding to the grid point nearest $\xi = 0$ and we set $A^* = 1$ as the nondimensional amplitude. Thus the Newton solve is applied to the nonlinear system

$$\boldsymbol{R}(\boldsymbol{\phi}; \bar{c}, b) = \boldsymbol{0}. \tag{99}$$

For the capacitance law

$$F(\phi) = \left(1 + \frac{\phi}{b}\right)^{-m}, \tag{100}$$

Since the nonlinearity enters through the antiderivative $G(\phi)$, we have

$$\frac{d}{d\phi}G(\phi) = F(\phi). \tag{101}$$

Hence the Jacobian of the unconstrained residual is

$$J_0(\boldsymbol{\phi}; \bar{c}, b) = S_- - 2I_M + S_+ - \bar{c}^2 D_2 \operatorname{diag}\big(F(\phi_1), \ldots, F(\phi_M)\big), \tag{102}$$

where I_M is the $M \times M$ identity matrix. It is immediately clear that the Jacobian is banded, with half-bandwith of $\bar{m}$

After imposing the boundary and normalization constraints, the corresponding rows of the Jacobian are replaced by

$$(J(\boldsymbol{\phi}; \bar{c}, b))_{1,:} = \boldsymbol{e}_1^\top, \tag{103}$$
$$(J(\boldsymbol{\phi}; \bar{c}, b))_{M,:} = \boldsymbol{e}_M^\top, \tag{104}$$
$$(J(\boldsymbol{\phi}; \bar{c}, b))_{j_0,:} = \boldsymbol{e}_{j_0}^\top, \tag{105}$$

where $\boldsymbol{e}_j$ denotes the j-th Euclidean basis vector. At each Newton iteration, we solve the linear system

$$J(\boldsymbol{\phi}^{(k)}; \bar{c}, b)\, \boldsymbol{\phi}_{\text{step}}^{(k)} = -\boldsymbol{R}(\boldsymbol{\phi}^{(k)}; \bar{c}, b), \tag{106}$$

and update the solution via

$$\boldsymbol{\phi}^{(k+1)} = \boldsymbol{\phi}^{(k)} + \boldsymbol{\phi}_{\text{step}}^{(k)}. \tag{107}$$

D. Lagrangian and Hamiltonian Structure of the Infinite LC-Ladder

This appendix derives the Lagrangian and Hamiltonian structure of the infinite LC-ladder network in the physical variables (n, t). This formulation underlies the symplectic time integrator introduced in Section 5.1.

We consider an infinite lattice indexed by $n \in \mathbb{Z}$. Let

$$\Phi_n(t) \in \mathbb{R}$$

denote the magnetic flux associated with the n^{th} node, so that the voltage is

$$V_n(t) = \frac{d}{dt}\Phi_n(t). \tag{108}$$

The current through the inductor between nodes n and $n+1$ is given by

$$I_n(t) = \frac{1}{\ell L_0}\big(\Phi_n(t) - \Phi_{n+1}(t)\big). \tag{109}$$

Inductive energy. The energy stored in the n^{th} inductor is

$$E_L^{(n)} = \frac{1}{2}\ell L_0 I_n^2 = \frac{1}{2\ell L_0}\big(\Phi_n - \Phi_{n+1}\big)^2. \tag{110}$$

Capacitive energy. The charge stored at node n is

$$Q_n(t) = C_0 G(V_n(t)). \tag{111}$$

The corresponding capacitor energy is

$$E_{\tilde{C}}^{(n)} = \int_0^{V_n(t)} Q_n(v)\,dv = C_0 \int_0^{V_n(t)} G(v)\,dv. \tag{112}$$

Since $V_n = \dot{\Phi}_n$, this may be written as a function of $\dot{\Phi}_n$:

$$E_{\tilde{C}}^{(n)} = C_0 \int_0^{\dot{\Phi}_n} G(v)\,dv. \tag{113}$$

The total Lagrangian is obtained by summing the capacitor (kinetic-type) and inductor (potential-type) energies over all nodes:

$$\mathcal{L}(\Phi, \dot{\Phi}) = \sum_{n\in\mathbb{Z}} \left[C_0 \int_0^{\dot{\Phi}_n} G(v)\,dv - \frac{1}{2\ell L_0}\big(\Phi_n - \Phi_{n+1}\big)^2 \right]. \tag{114}$$

To now obtain the corresponding Hamiltonian, we can use the Legendre transform. The momentum conjugate to Φ_n is

$$\Pi_n(t) = \frac{\partial \mathcal{L}}{\partial \dot{\Phi}_n} = C_0 G(\dot{\Phi}_n) = Q_n(t), \tag{115}$$

using the definition of the charge stored in the n^{th} capacitor given in (7). Thus the conjugate momentum is precisely the capacitor charge, which gives a direct physical interpretation of the canonical variables.

Assuming the constitutive relation can be inverted, we may express $\dot{\Phi}_n$ as a function of Π_n.

The Hamiltonian is defined by the Legendre transform

$$\mathcal{H}(\Phi, \Pi) = \sum_{n\in\mathbb{Z}} \Pi_n \dot{\Phi}_n - \mathcal{L}(\Phi, \dot{\Phi}), \tag{116}$$

where $\dot{\Phi}_n = \dot{\Phi}_n(\Pi_n)$.

Since the conjugate momentum is precisely the capacitor charge,

$$\Pi_n = Q_n = C_0 G(\dot{\Phi}_n),$$

it is natural to eliminate $\dot{\Phi}_n$ in favor of the canonical variable Q_n. Let $V(q)$ denote the inverse constitutive relation defined implicitly by

$$q = C_0 G(V(q)).$$

Then the Hamiltonian may be written entirely in terms of (Φ_n, Q_n) as

$$\mathcal{H}(\boldsymbol{\Phi}, \boldsymbol{Q}) = \sum_{n\in\mathbb{Z}} \left[Q_n V(Q_n) - C_0 \int_0^{V(Q_n)} G(v)\, dv + \frac{1}{2\ell L_0} \big(\Phi_n - \Phi_{n+1}\big)^2 \right]. \tag{117}$$

Equivalently, defining

$$\Psi_n(Q_n) = Q_n V(Q_n) - C_0 \int_0^{V(Q_n)} G(v)\, dv,$$

the Hamiltonian takes the form

$$\mathcal{H}(\boldsymbol{\Phi}, \boldsymbol{Q}) = \sum_{n\in\mathbb{Z}} \left[\Psi(Q_n) + \frac{1}{2\ell L_0} \big(\Phi_n - \Phi_{n+1}\big)^2 \right]. \tag{118}$$

Notice the Hamiltonian is separable, which allows us to use the Störmer Verlet integration method.

$$\mathcal{H}(\boldsymbol{\Phi}, \boldsymbol{Q}) = T(\boldsymbol{Q}) + V(\boldsymbol{\Phi}).$$

Hamilton's equations. The canonical equations are

$$\dot{\Phi}_n = \frac{\partial \mathcal{H}}{\partial Q_n} = V(Q_n), \tag{119}$$

$$\dot{Q}_n = -\frac{\partial \mathcal{H}}{\partial \Phi_n} = \frac{1}{\ell L_0} \big(\Phi_{n-1} - 2\Phi_n + \Phi_{n+1}\big). \tag{120}$$

The symplectic Störmer–Verlet method used in Section 5.1 implements the above dynamics. In the absence of forcing and dissipation, this method preserves the symplectic structure and exhibits near-conservation of the total energy over long time intervals [27]. Using the constitutive relations

$$Q_n = C_0 \int_0^{V_n(t)} F(v)\, dv, \qquad I_n = \frac{1}{\ell L_0} (\Phi_n - \Phi_{n+1}),$$

equation (120) becomes

$$\dot{Q}_n = I_{n-1} - I_n, \tag{121}$$

which is precisely Kirchhoff's current law at node n. Similarly, differentiating the definition of I_n and using (119) yields

$$\dot{I}_n = \frac{V_n - V_{n+1}}{\ell L_0}, \tag{122}$$

which recovers the inductor relation.